nature materials

Article

https://doi.org/10.1038/s41563-023-01700-3

Localized high-concentration electrolytes get more localized through micelle-like structures

In the format provided by the authors and unedited

Contents

Supplementary Fig. 1 | Radial distribution function (RDF) and coordination number (CN) plots. 3

Supplementary Fig. 2 | DME-Li^+ coordination. 4

Supplementary Fig. 3 | Binding energies (BE) of Li^+ to salt anion, solvent, and diluent molecules. 5

Supplementary Fig. 4 | Definitions of salt-solvent clusters based on FSI^- to Li^+ CNs. 6

Supplementary Fig. 5 | Salt-solvent clusters in HCEs and LCE. 7

Supplementary Fig. 6 | Salt-solvent cluster ratios as functions of temperatures in LHCE (LiFSI-1.2DME-2TFEO). 8

Supplementary Fig. 7 | Salt-solvent cluster ratios as functions of temperatures in HCEs 9

Supplementary Fig. 8 | Raman spectra of LHCE as a function of TFEO concentration 10

Supplementary Fig. 9 | MD simulations of LHCE (LiFSI-1.2DME-8TFEO) 11

Supplementary Fig. 10 | DFT-calculated reduction potentials for different salt clusters 12

Supplementary Table 1 | SEI comparison of elements from XPS 14

Supplementary Fig. 12 | Carbon peak depth profiling of HCE (LiFSI-1.2DME) at different temperatures 15

Supplementary Fig. 13 | Ionic conductivity of LiFSI-DMC-TTE electrolyte 16

Supplementary Fig. 14 | Structure factors, S(q), of LiFSI-1.2DME-xTFEO electrolytes 17

Supplementary Fig. 15 | Ternary phase diagrams of different LHCE systems 18

Supplementary Fig. 16 | Coulombic efficiency (CE) voltage profile of LiFSI-1.5DMC-3.07TTE LHCE. 19

Supplementary Table 2 | CE values of different LHCEs in literature 20

Supplementary Fig. 17 | Cu-NMC811 coin cell cycling performance for elected LHCEs 21

Supplementary Fig. 18 | Atom types and atomic charges used in MD simulations 22

Supplementary Fig. 19 | DFT- vs force field (FF)-calculated binding energies 23

Supplementary Table 3 | MD data of LCE (1 M LiFSI in DME). 24

Supplementary Table 4 | MD data of HCE (4 M LiFSI in DME). 25

Supplementary Tables 5 | MD data of 1M $LiPF_6$ in EC-EMC (3-7 by vol). 26

Supplementary Table 6 | MD-calculated ratios of SSIP, CIP, AGG and AGG+ 27

Supplementary Fig. 20 | MD-simulated structure of 4 LiFSI molecules in TFEO matrix (with 200 TFEO molecules) for different scaled charges 28

Supplementary Fig. 21 | MD simulations of LHCE starting from several different initial configurations. 29

Supplementary Table 7 | Table list of number of LiFSI, DME, and/or TFEO in the simulation cells of different systems for MD simulations 30

Supplementary Fig. 22 | Perspective views of MD simulations using different simulation cells at room temperature for LHCE (LiFSI-1.2DME-2TFEO) 31

Supplementary Fig. 23 | Statistics of coordination numbers (CN) and aggregation ratios for LCE (LiFSI-9DME) 32
Supplementary Fig. 24 | Statistics of coordination numbers (CN) and aggregation ratios for HCE (LiFSI-1.4DME) 33
Supplementary Fig. 25 | Statistics of coordination numbers (CN) and aggregation ratios for HCE (LiFSI-1.2DME) 34
Supplementary Fig. 26 | Statistics of coordination numbers (CN) and aggregation ratios for LHCE (LiFSI-1.2DME-2TFEO) 35
Supplementary Fig. 27 | Time-averaged coordination number (CN) and aggregate types as a function of temperature for an extended 10.0 ns NPT simulation of LHCE (LiFSI-1.2DME-2TFEO) 36
Supplementary Fig. 28 | MD tests on different cutoffs used for calculating salt-solvent cluster ratios 37
References 38

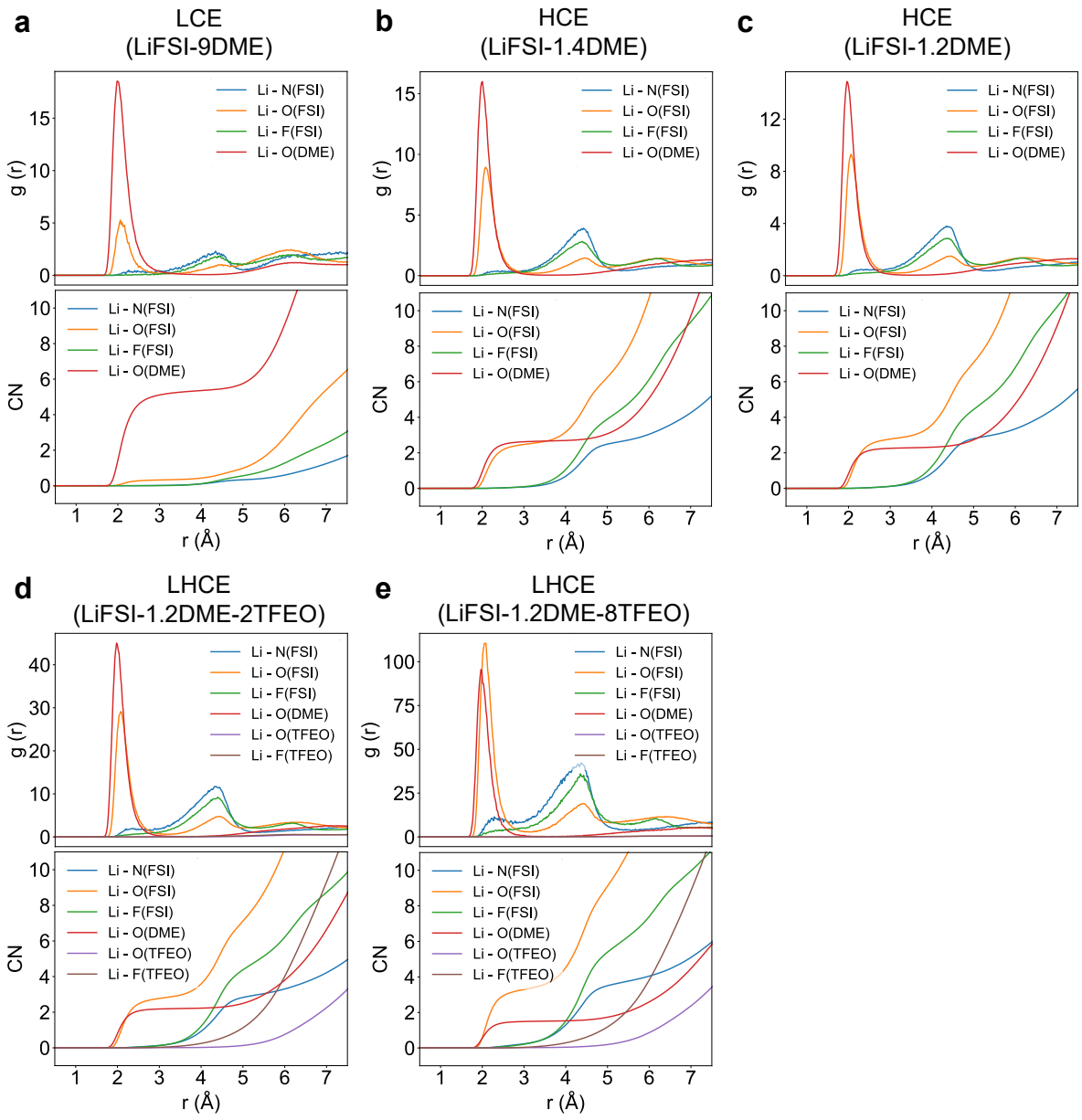

Supplementary Fig. 1 | Radial distribution function (RDF) and coordination number (CN) plots. a-c, Time averaged RDF and CN as functions of distances between Li^+ and N, O and F atoms in FSI^- and DME molecules for **a**, LCE (LiFSI-9DME), **b**, HCE (LiFSI-1.4DME), and **c**, HCE (LiFSI-1.2DME) obtained through molecular dynamics (MD) simulations and analysis at 25 °C. In LCE, the Li^+ solvation shell is mainly composed of O atoms from DME, while both FSI^- and DME contribute significantly to the Li^+ solvation shell in HCEs. **d-e**, RDF and CN as functions of distances between Li^+ and N, O and F atoms in FSI^-, DME and TFEO molecules for, **d**, LHCE (LiFSI-1.2DME-2TFEO) and, **e**, LHCE (LiFSI-1.2DME-8TFEO) obtained through MD simulations and analysis at 25 °C. In LHCEs, the Li^+ solvation shell is mainly composed of O atoms from FSI^- and DME with minimal participation of O/F atoms from TFEO molecules. The cutoff for the Li^+ solvation shell is set to 2.8 Å.

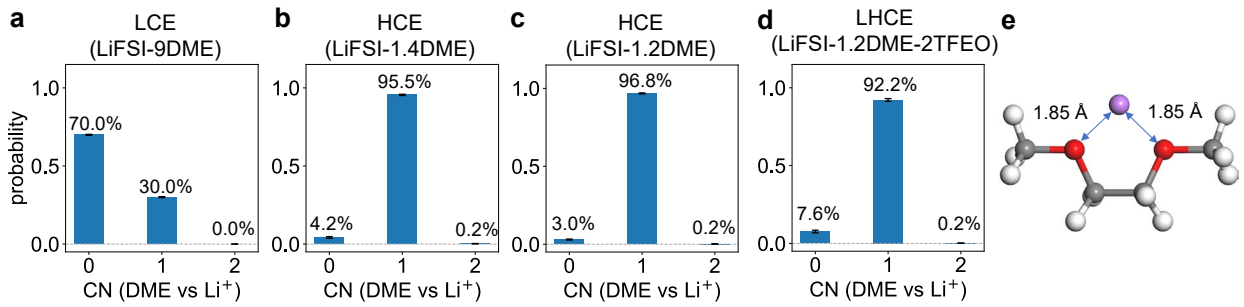

Supplementary Fig. 2 | DME-Li$^+$ coordination. The probability distributions of DME *vs* Li$^+$ coordination numbers (CN) in **a**, LCE (LiFSI-9DME), **b**, HCE (LiFSI-1.4DME), **c**, HCE (LiFSI-1.2DME), and **d**, LHCE (LiFSI-1.2DME-2TFEO). **e**, DFT-optimized geometry of DME molecule coordinating with one Li$^+$. It is seen that for almost all DME molecules (≥ 99.8%), each of them is coordinating with up to one Li$^+$, independent of the salt concentration. This is because when DME molecule is coordinated with one Li$^+$ through its two ether oxygen atoms there is no coordination site for a second Li$^+$. There are more DME molecules that are not coordinated with any Li$^+$ (CN = 0) in LCE compared to HCEs, which is consistent with what is shown in Fig. 3a. The probabilities in **a**-**d** are calculated based on the counting of DME molecules that have different coordination numbers to Li$^+$ during production runs. All the reported values are averaged for 4 ns production run, $\langle probability(4\,ns)\rangle$, with n>10,000 (number of MD frames multiplying number of DME molecules in the systems). We define the error bar as the difference between the maximum and minimum in the time-averaged values, $error = \pm(\,max\{\langle probability(t)\rangle\} - min\{\langle probability(t)\rangle\})$, from 2 ns to 4 ns during production runs.

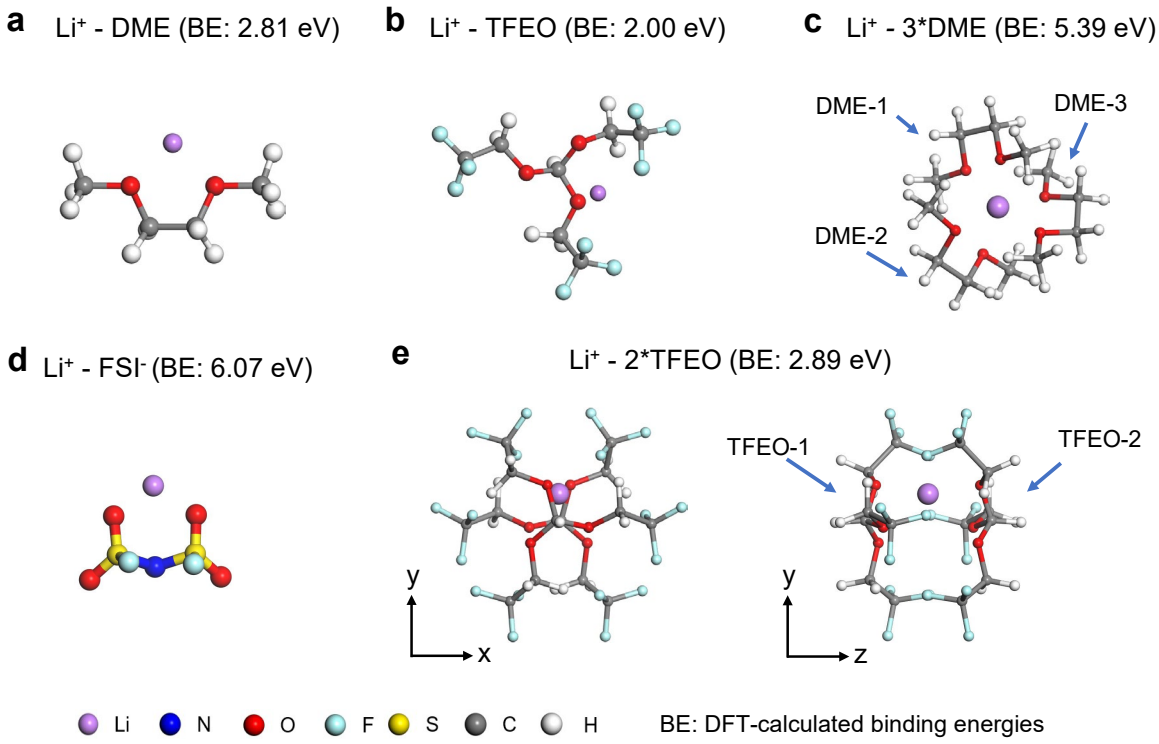

Supplementary Fig. 3 | Binding energies (BE) of Li^+ to salt anion, solvent, and diluent molecules. DFT-optimized geometry of **a**, Li^+ coordinating to one DME molecule, **b**, Li^+ coordinating with one TFEO molecule, **c**, Li^+ coordinating to three DME molecules, **d**, Li^+-FSI^-, and **e**, Li^+ coordinating to two TFEO molecules. BE for each case is given accordingly, which is defined as $E_{BE} = E_{Li^+} + E_{mol} - E_{bound}$, where E_{Li^+} denotes the energy of Li^+, E_{mol} denotes the energy of the anion (FSI^-), solvent (DME) cluster, or diluent (TFEO) cluster, and E_{bound} denotes the energy of the bound system.

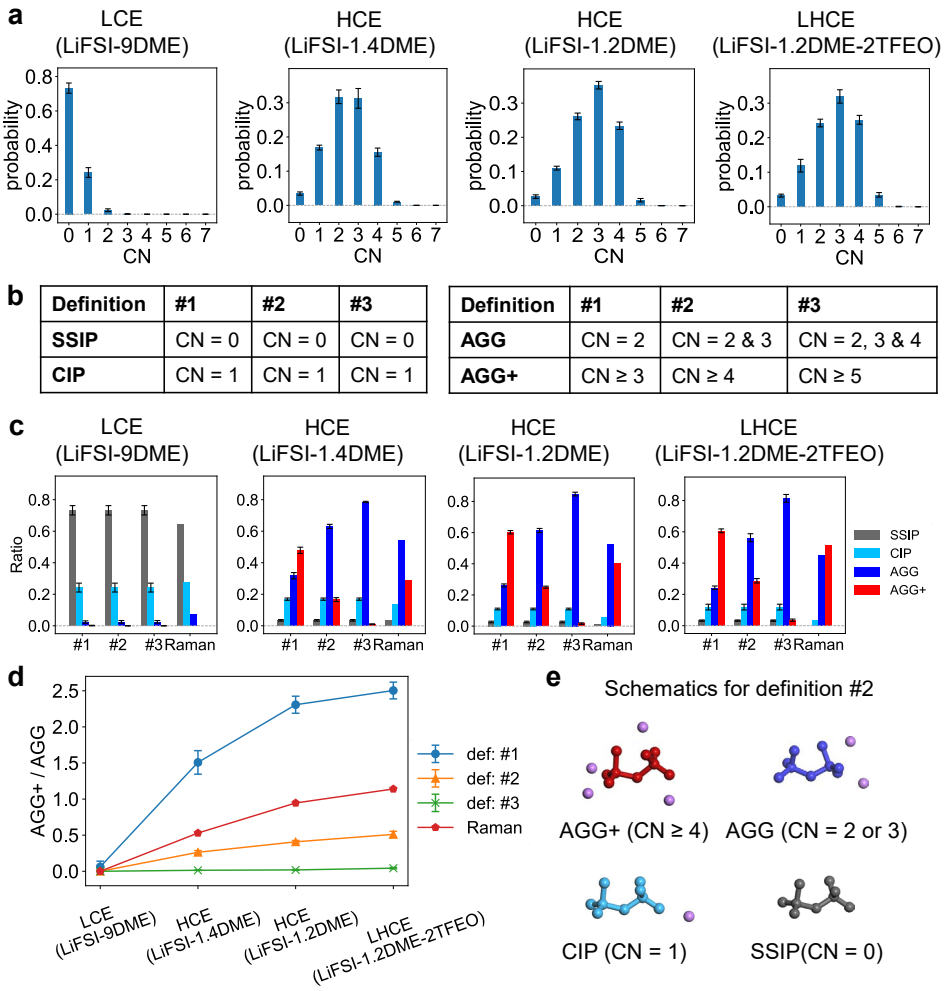

Definition	#1	#2	#3
SSIP	CN = 0	CN = 0	CN = 0
CIP	CN = 1	CN = 1	CN = 1

Definition	#1	#2	#3
AGG	CN = 2	CN = 2 & 3	CN = 2, 3 & 4
AGG+	CN ≥ 3	CN ≥ 4	CN ≥ 5

Supplementary Fig. 4 | Definitions of salt-solvent clusters based on FSI^- to Li^+ CNs. a, MD-calculated probability distributions of coordination number of FSI^- *vs* Li^+ pair in LCE (LiFSI-9DME), HCE (LiFSI-1.4DME), HCE (LiFSI-1.2DME) and LHCE (LiFSI-1.2DME-2TFEO), respectively, at 25 °C. **b**, Three possible definitions (#1, #2 and #3) that are used to count SSIP, CIP, AGG, and AGG+ based on MD simulations and analyses. **c**, Calculated ratios of SSIP, CIP, AGG, and AGG+ in LCE, HCEs and LHCE at 25 °C based on three different definitions and compared to results from Raman deconvolution analysis. **d**, Comparison among the ratios of AGG+/AGG calculated using different computational definitions and through Raman deconvolution analysis. It is seen that definition #2 gives the most accurate description of the salt-solvent cluster ratios when compared with the ratios calculated through Raman. Thus, definition #2 is used in this work for all analyses. **e**, Schematic and CNs for SSIP, CIP, AGG, and AGG+ using the definition #2 for the solvent-salt clusters. The probabilities in **a** and **c** are calculated based on the counting of DME molecules that have different coordination numbers to Li^+ during production runs. All the reported values are averaged for 4 ns production run, $\langle CN(4\ ns)\rangle$ or $\langle probability(4\ ns)\rangle$, with n>10,000 (number of MD frames multiplying number of LiFSI molecules in the systems). We define the error bar as the difference between the maximum and minimum in the time-averaged values, $error = \pm(\ max\{\langle CN(t)\rangle\} - min\{\langle CN(t)\rangle\})$, or $error = \pm(\ max\{\langle probability(t)\rangle\} - min\{\langle probability(t)\rangle\})$, from 2 ns to 4 ns during production runs.s

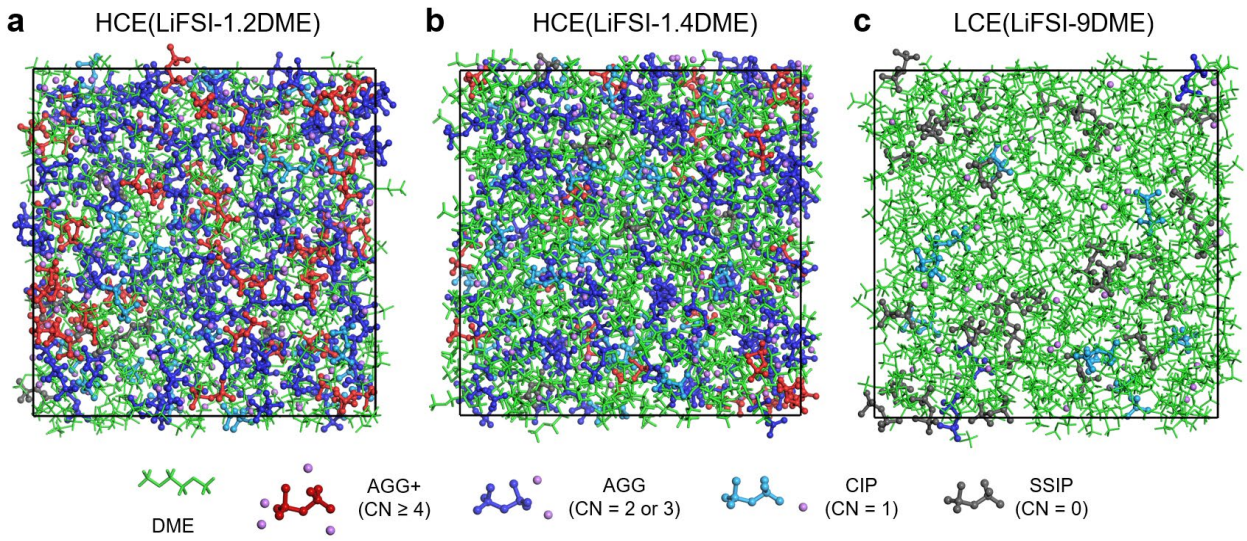

Supplementary Fig. 5 | Salt-solvent clusters in HCEs and LCE. Snapshots at the end of MD simulations for, **a**, HCE (LiFSI-1.2DME), **b**, HCE (LiFSI-1.4DME) and **c**, LCE (LiFSI-9DME). All LiFSI and DME molecules are shown in the snapshots. Different types of salt-solvent clusters (AGG+, AGG, CIP, and SSIP) are color-encoded for demonstration of their spatial distributions. The black lines indicate the boundaries of the simulation cells.

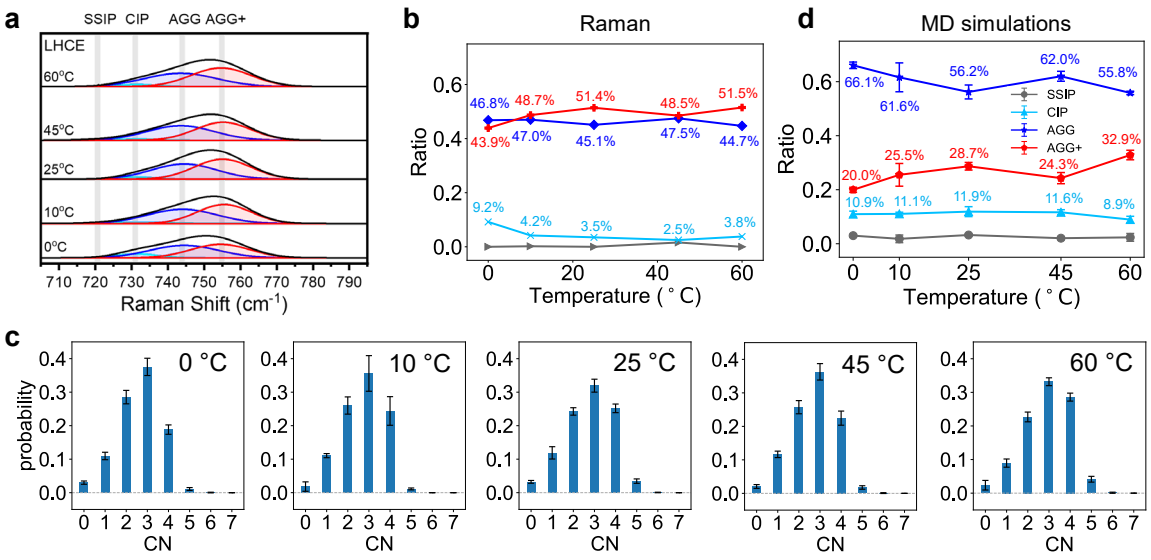

Supplementary Fig. 6 | Salt-solvent cluster ratios as functions of temperatures in LHCE (LiFSI-1.2DME-2TFEO). a, Raman peak deconvolution of Li^+-FSI^- interactions and, **b**, corresponding calculated ratios of SSIP, CIP, AGG and AGG+ for LHCE (LiFSI-1.2DME-2TFEO) at different temperatures (0 °C, 10 °C, 25 °C, 45 °C, and 60 °C). **c**, Probability distributions of coordination number of FSI^- *vs* Li^+ pair in LHCE at different temperatures calculated from MD simulations and analysis. **d**, MD-calculated probabilities of SSIP, CIP, AGG, and AGG+ at different temperatures for LHCE. Ratio percentages are included for CIP, AGG, and AGG+ of LHCE at different temperatures for both Raman and MD. The probabilities in **c** are calculated based on the counting of DME molecules that have different coordination numbers to Li^+ during production runs. All the reported values are averaged for 4 ns production run, $\langle probability(4\ ns)\rangle$, with n=16,000 (200 frames multiplying 80 LiFSI molecules). We define the error bar as the difference between the maximum and minimum in the time-averaged values, $error = \pm(\ max\{\langle probability(t)\rangle\} - min\{\langle probability(t)\rangle\})$, from 2 ns to 4 ns during production runs.

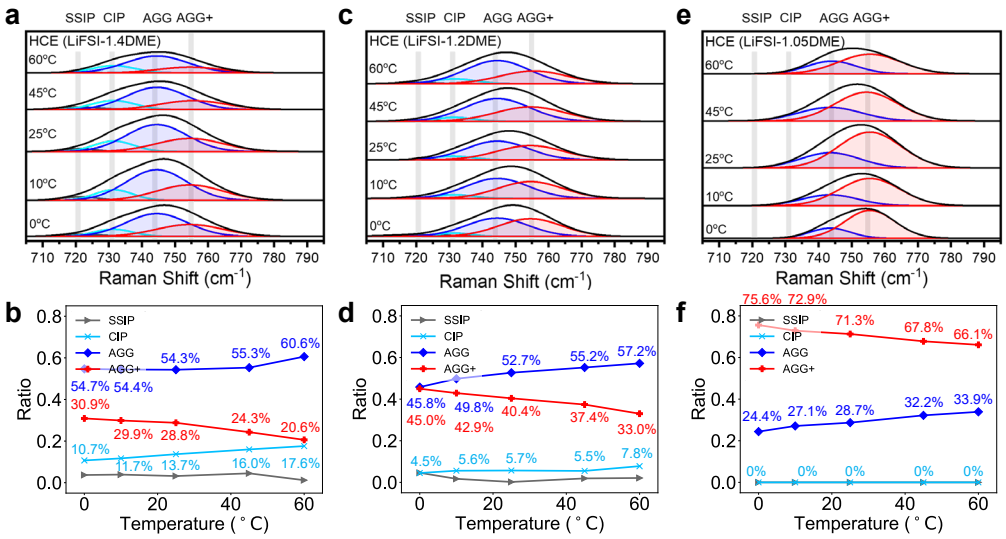

Supplementary Fig. 7 | Salt-solvent cluster ratios as functions of temperatures in HCEs. (Top) Raman peak deconvolution of Li^+-FSI^- interactions and (bottom) corresponding calculated ratios of SSIP, CIP, AGG and AGG+ for **a-b**, HCE (LiFSI-1.4DME), **c-d**, HCE (LiFSI-1.2DME), and **e-f**, binary electrolyte near the solubility limit (LiFSI-1.05DME). Ratio percentages are included for all CIP, AGG, and AGG+ structures at different temperatures of each electrolyte.

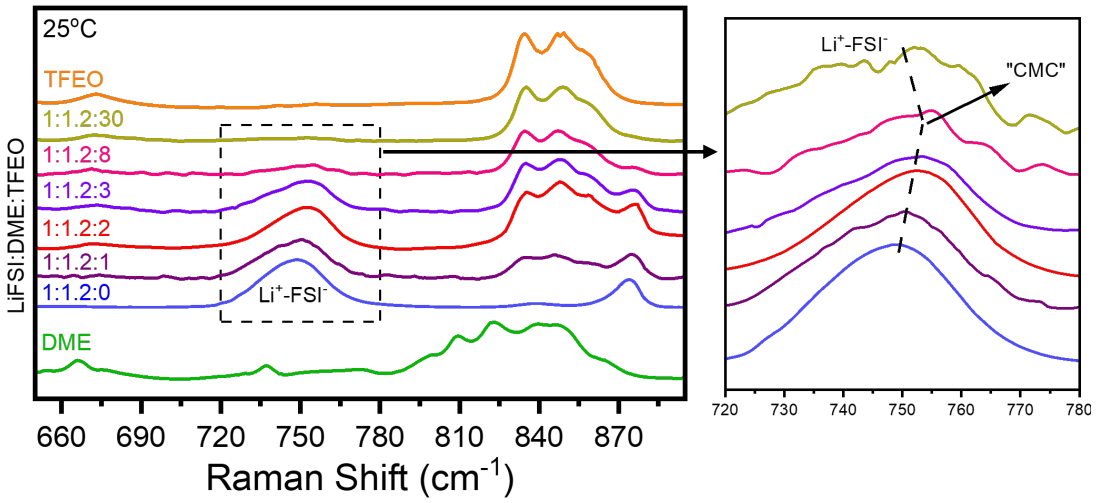

Supplementary Fig. 8 | Raman spectra of LHCE as a function of TFEO concentration. Raman spectra at 25°C for (bottom to top) DME (green), HCE (LiFSI-1.2DME as blue), LHCEs of LiFSI-1.2DME-*x*TFEO molar ratios (*x* between 1 and 30), and TFEO (orange). Blue-shifting can be seen for Li^+-FSI^- coordination peak when TFEO concentration increases up to *x*=8, which corresponds to more AGG+ in LHCE, and red-shifting can be seen for Li^+-FSI^- coordination peak when TFEO concentration further increases, suggesting damage of micelle-like structures.

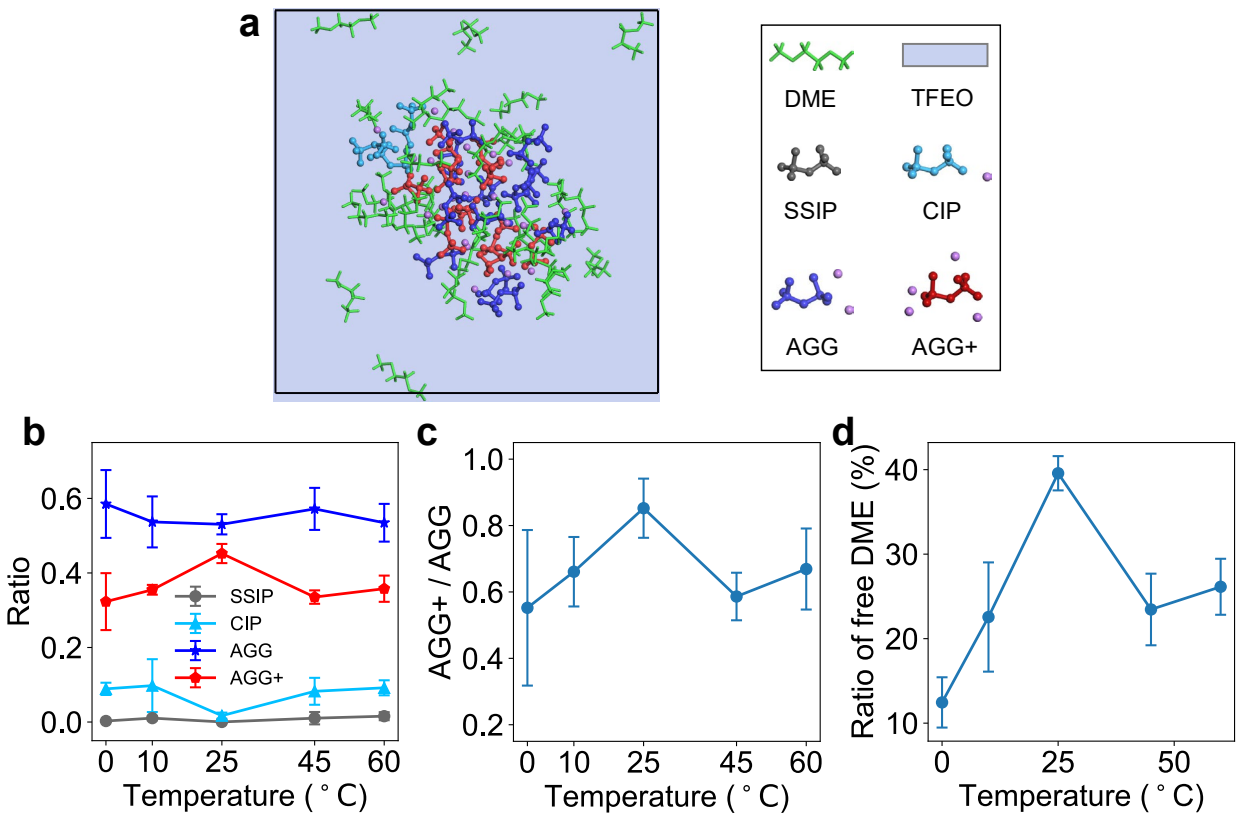

Supplementary Fig. 9 | MD simulations of LHCE (LiFSI-1.2DME-8TFEO). a, MD trajectory snapshot showing the spatial distributions of salt-solvent clusters in LHCE (LiFSI-1.2DME-8TFEO). The green stick model stands for DME molecule, light blue area for TFEO network, red ball-and-stick model for AGG+, blue ball-and-stick model for AGG, cyan ball-and-stick model for CIP, and dark grey ball-and-stick model for SSIP, and the square black lines indicate simulation boundaries. **b**, MD-calculated ratios of SSIP, CIP, AGG, and AGG+ as functions of temperature in LHCE (LiFSI-1.2DME-8TFEO). **c**, MD-calculated AGG+/AGG ratio as function of temperature in LHCE (LiFSI-1.2DME-8TFEO). **d**, Ratio of free DME molecules (not coordinating with any Li^+) as a function of temperature in LHCE (LiFSI-1.2DME-8TFEO). All the reported values in **b-d** are averaged for 4 ns production run, $\langle probability(4\ ns)\rangle$, with n=12,500 (500 frames multiplying 25 LiFSI molecules). We define the error bar as the difference between the maximum and minimum in the time-averaged values, $error = \pm(\ max\{\langle probability(t)\rangle\} - min\{\langle probability(t)\rangle\})$, from 2 ns to 4 ns during production runs.

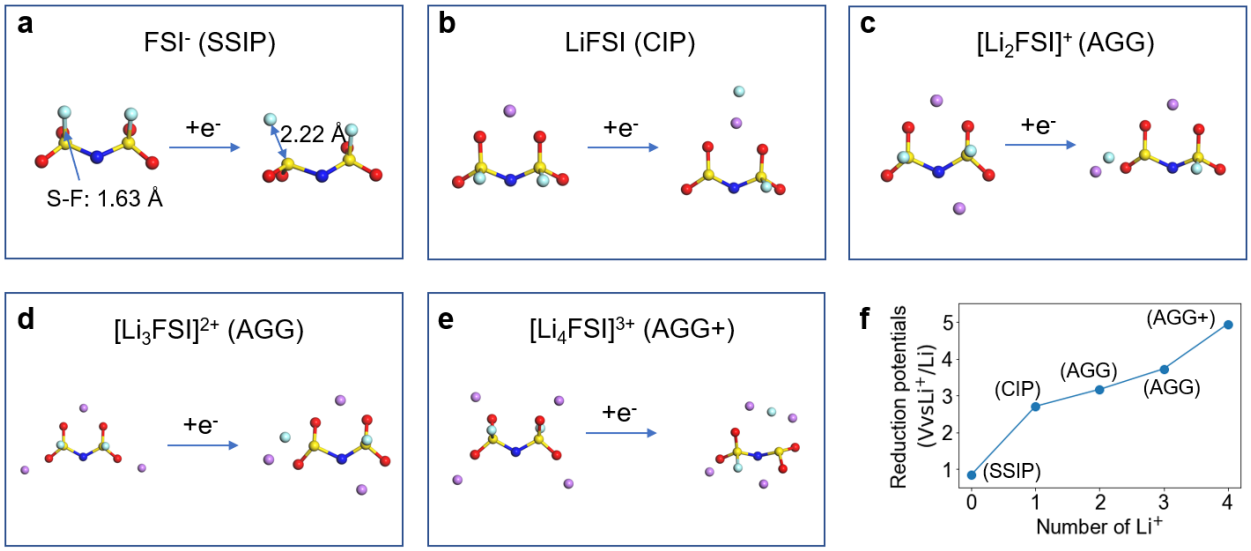

Supplementary Fig. 10 | DFT-calculated reduction potentials for different salt clusters. Reduction reactions and corresponding reduction potentials (*vs* Li^+/Li) for **a**, FSI^-, **b**, LiFSI, **c**, $[Li_2FSI]^+$, **d**, $[Li_3FSI]^{2+}$, and **e**, $[Li_4FSI]^{3+}$. The aggregate types (SSIP, CIP, AGG, and AGG+) are shown in parentheses accordingly. **f**, Reduction potentials as functions of the number of Li^+ ions that are coordinated with one FSI^-.

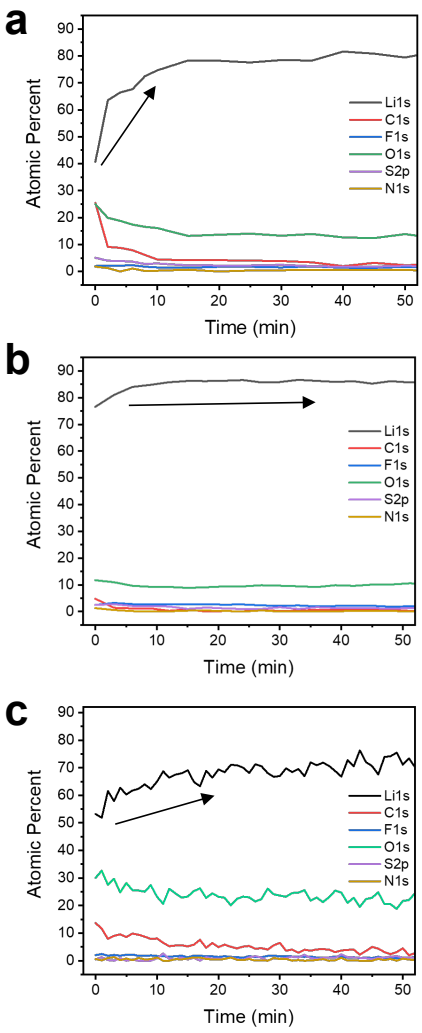

Supplementary Fig. 11 | Elemental depth profiling. XPS depth profiles of stripped (i.e., delithiated) Li foils after formation cycles at **a**, 10 °C, **b**, 25 °C, and **c**, 45 °C. At 25 °C, a higher Li atomic concentration and brief change in its concentration over time of sputtering reveals its thin thickness in comparison to the decomposition surface seen at 10 °C and 45 °C. At 10 °C, the change in Li concentration changes rapidly over the first 10-15 minutes of sputtering, followed by relatively steady composition after further sputter. At 45 °C, a slow and steady change in composition is seen over the extent of sputtering, revealing either thick or highly non-uniform decomposition surface.

Supplementary Table 1 | SEI comparison of elements from XPS. XPS depth profile atomic ratios of fluorine, sulfur, and nitrogen in comparison to carbon, averaged over the range of the SEI for each electrolyte and temperature (a cut-off of 20 minutes sputtering was used for depth profiles with linear trends, 10 °C and 45 °C). The higher ratio of F/C, S/C and N/C ratio at 25 °C suggests more inorganic and less organic material in the decomposition surface.

	10 °C	25 °C	45 °C
F:C ratio	0.25	1.07	0.24
S:C ratio	0.45	1.86	0.097
N:C ratio	0.074	1.63	0.086

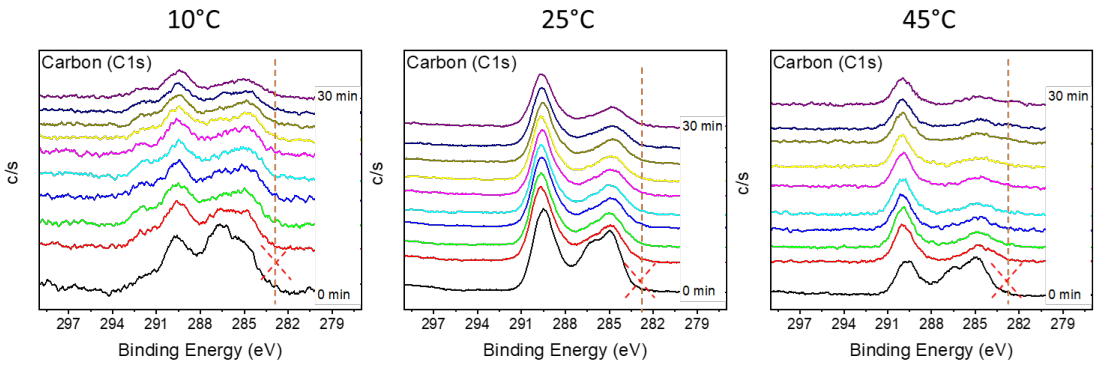

Supplementary Fig. 12 | Carbon peak depth profiling of HCE (LiFSI-1.2DME) at different temperatures. XPS depth profiles of stripped (i.e., delithiated) Li foils after formation cycles for carbon at 10 °C, 25 °C, and 45 °C. Obvious C-Li bonds (Fig. 5d) and C-F bonds (Fig. 5f) in SEI formed only at 10 ºC were found. Moreover, C-Li bonds almost do not exist in HCE without TFEO. Those suggest Li-C formation is due to the decomposition of TFEO and more organic components formed in the SEI at 10 ºC would permit further decomposition mechanisms of the diluent or solvent, resulting in obvious C-F and C-Li peaks.

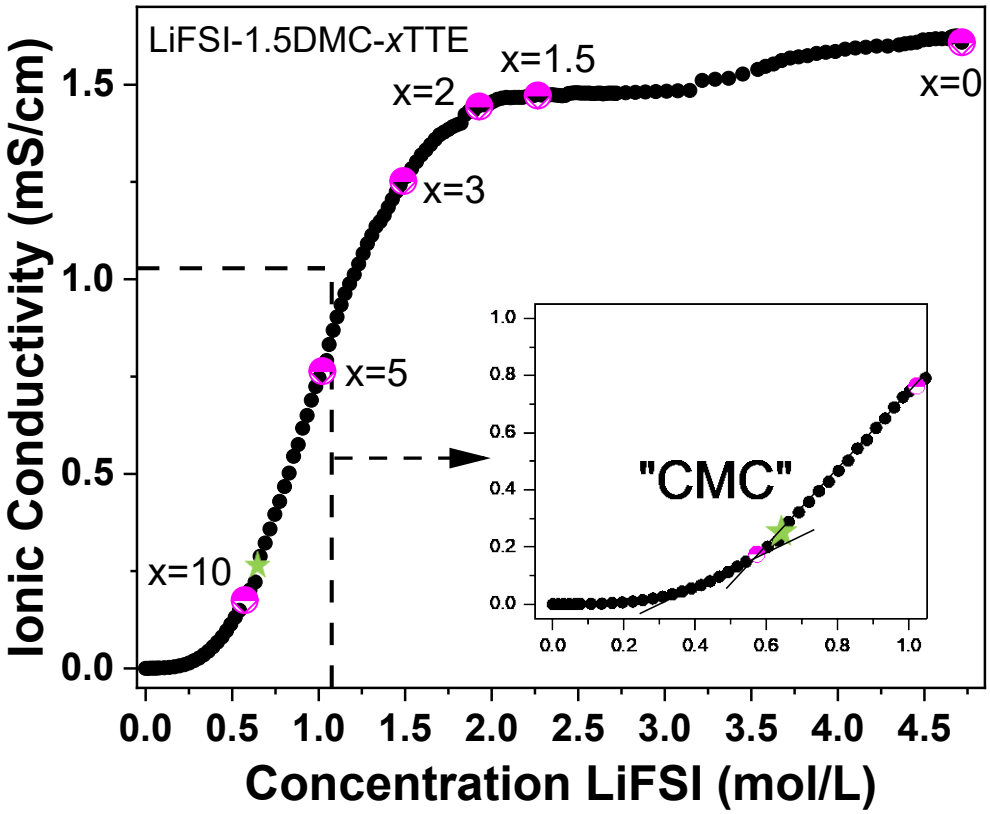

Supplementary Fig. 13 | Ionic conductivity of LiFSI-DMC-TTE electrolyte. Ionic conductivities of LiFSI-1.5DMC-*x*TTE solutions as a function of LiFSI salt concentration, acquired between 21-22 °C. Specific solutions (pink circles), as well as the "CMC" (in the inset as a green star) are noted.

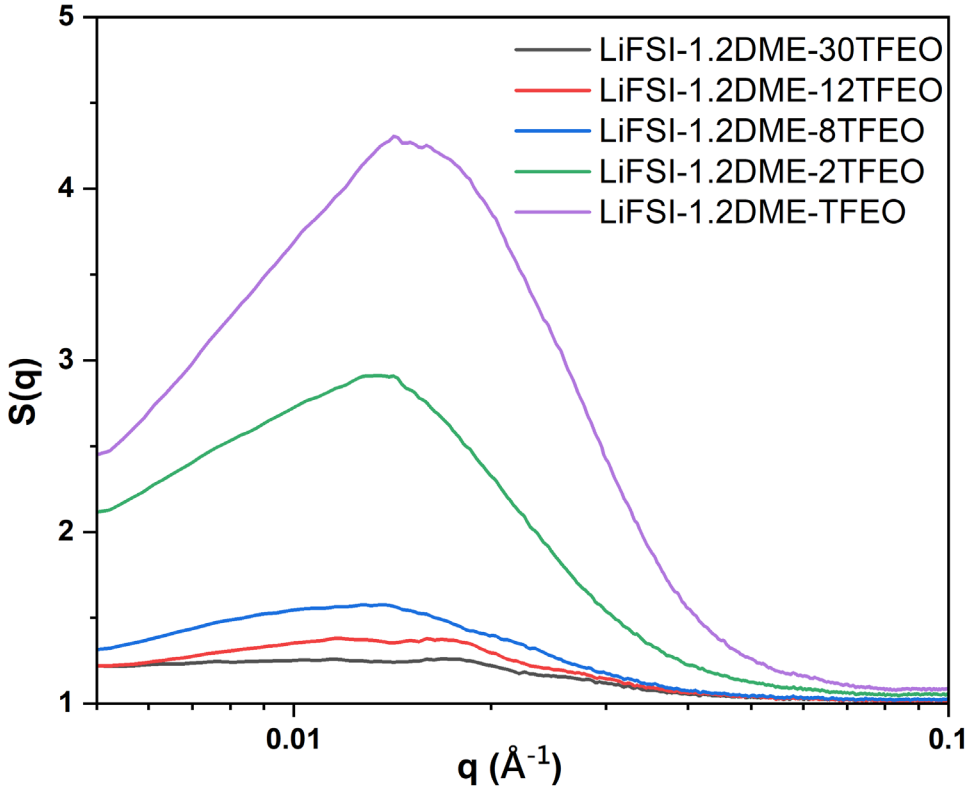

Supplementary Fig. 14 | Structure factors, S(q), of LiFSI-1.2DME-xTFEO electrolytes. Structure factor derived from SAXS patterns with TFEO in different molar ratios in LHCEs (x = 1, 2, 8, 12 and 30). Peak intensity increases when diluent concentration decreases, suggesting more micelle-like structures are interacting with each other.

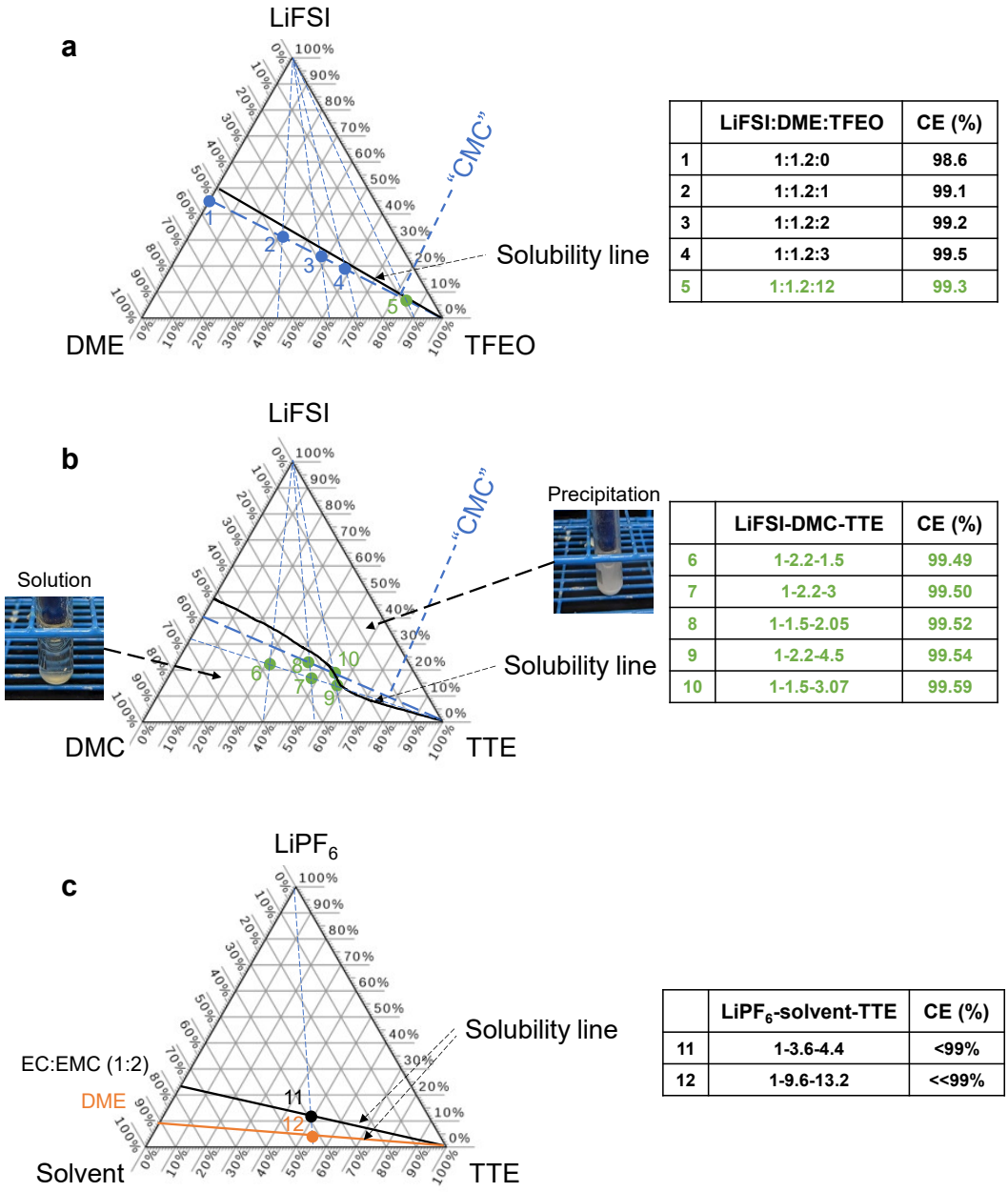

	LiFSI:DME:TFEO	CE (%)
1	1:1.2:0	98.6
2	1:1.2:1	99.1
3	1:1.2:2	99.2
4	1:1.2:3	99.5
5	1:1.2:12	99.3

	LiFSI-DMC-TTE	CE (%)
6	1-2.2-1.5	99.49
7	1-2.2-3	99.50
8	1-1.5-2.05	99.52
9	1-2.2-4.5	99.54
10	1-1.5-3.07	99.59

	$LiPF_6$-solvent-TTE	CE (%)
11	1-3.6-4.4	<99%
12	1-9.6-13.2	<<99%

Supplementary Fig. 15 | Ternary phase diagrams of different LHCE systems. a, LiFSI-DME-TFEO.[1] **b**, LiFSI-DMC-TTE. **c**, $LiPF_6$-DME-TTE and $LiPF_6$-solvent-TTE (solvent as DME in orange, EC-EMC (1:2 by mole) in black).[2] The electrolyte formulation (molar ratio) and corresponding CE values are shown in the tables. Electrolyte formulations highlighted in green were tested in this work, utilizing the modified Aurbach (i.e., "Method 3"), referred elsewhere.[3] All other CE values are from literature, using similar methods. In the LiFSI-DMC-TTE system, the solubility line was approximated by experiments here and in literature,[4] as exemplified with the solution and precipitation images.

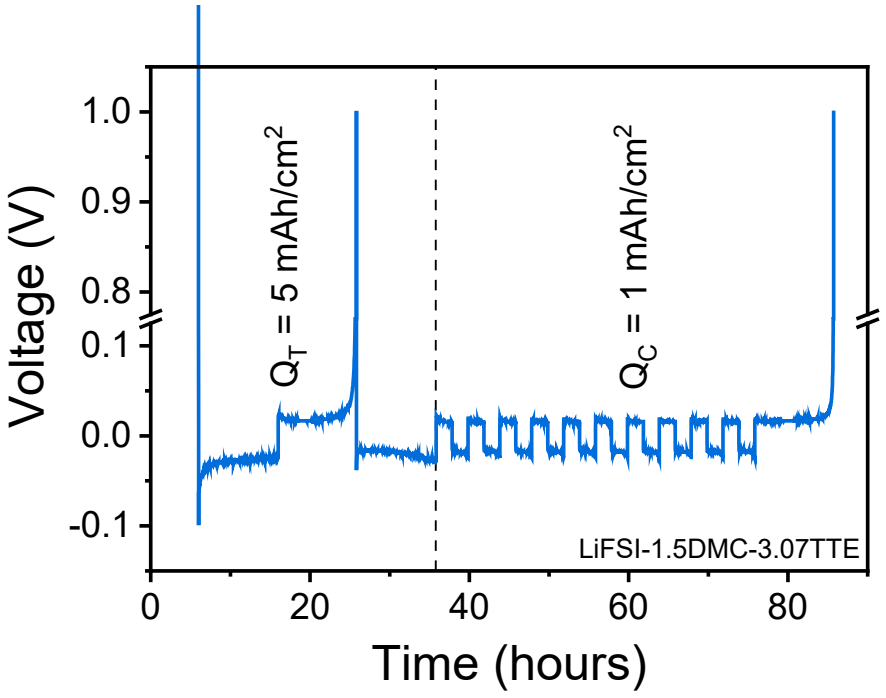

Supplementary Fig. 16 | Coulombic efficiency (CE) voltage profile of LiFSI-1.5DMC-3.07TTE LHCE. Coulombic efficiency averaged 99.59% over the 10 cycles. Q_T refers to capacity during formation cycles, while Q_C refers to capacity during CE-measured cycles. This CE testing design is based on the modified Aurbach (i.e., "Method 3"), referred elsewhere.[3]

Supplementary Table 2 | CE values of different LHCEs in literature. All CE values are accomplished in Li||Cu cells. Capacity, current, and number of cycles ran are included. Generally, CE would increase with increasing cycle numbers due to the formation of initial SEIs on Cu surfaces.

Electrolyte	Capacity (mAh/cm^2)	Current (mA/cm^2)	Cycles Ran	CE	Ref.
LiFSI-DMC-TTE (1-1.5-1.5 by mole)	**1**	**0.2**	**50**	**99.05**	[4]
LiFSI-DME-BTFE (1-1.2-3 by mole)	**1**	**0.5**	**10**	**99.4**	[5]
LiFSI-DME-BTFEC (1-1.2-3 by mole)	**1**	**0.5**	**10**	**96.8**	[5]
LiFSI-DME-TFEB (1-1.4-3 by mole)	**1**	**0.5**	**10**	**95.4**	[5]
LiFSI-DME-TFEO (1-1.2-3 by mole)	**1**	**0.5**	**10**	**99.5**	[5,6]
LiFSI-DME-TTE (1-1.2-3 by mole)	**1**	**0.5**	**10**	**99.5**	[5]
LiFSI-DME-TTE (1-1.2-3 by mole)	**1**	**0.5**	**300**	**99.3**	[7]
LiTFSI-DME-DOL-TME (1-1.5-1.5-6 by mole)	**1**	**0.5**	**10**	**99.13**	[8]
2.5M LiFSI in DMC-BTFE (1-1 by mole)	**1**	**0.5**	**10**	**99.5**	[9]
0.4M LiTFSI + 0.4M LiNO3 + 0.1M LiHFDF in DME-DOL-TFMTMS (48-17-35 by vol)	**1**	**0.5**	**100**	**98.5**	[10]
1M LiFSI in OFE-DME (1-5 by mole)	**1**	**0.5**	**250**	**99.3**	[11]
1M LiFSI in isoxazole-TTE (1-4.5 by vol) + 10 wt.% FEC	**1**	**1**	**10**	**98.6**	[12]
LiFSI-DME-FEC-OFE (1-1-1.4-3 by mole)	**2**	**1**	**200**	**98.9**	[13]
1.2M LiFSI in TEP-BTFE (1-3 by mole)	**1**	**0.5**	**10**	**99.2**	[14]
LiFSI-TMS-TTE (1-3-3 by mole)	**1**	**0.5**	**150**	**98.8**	[15]

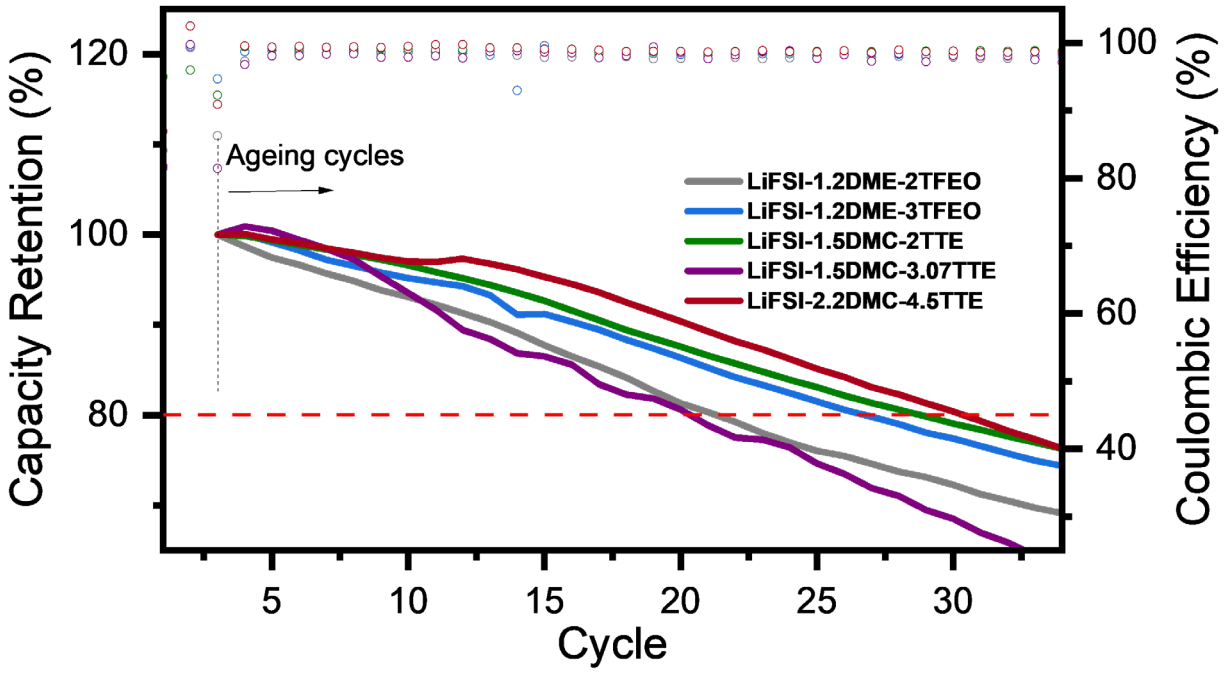

Supplementary Fig. 17 | Cu-NMC811 coin cell cycling performance for elected LHCEs. Coulombic efficiency and discharge capacity normalized from the first aging cycle show for the best performing LHCEs from CE tests (Supplementary Fig. 16). Cycling protocol followed the same process as Li-NMC811 coin cell tests. Dashed lines denote cycle in which the capacity retention falls below 80%.

MD Simulation Details

1. Force field and its validation

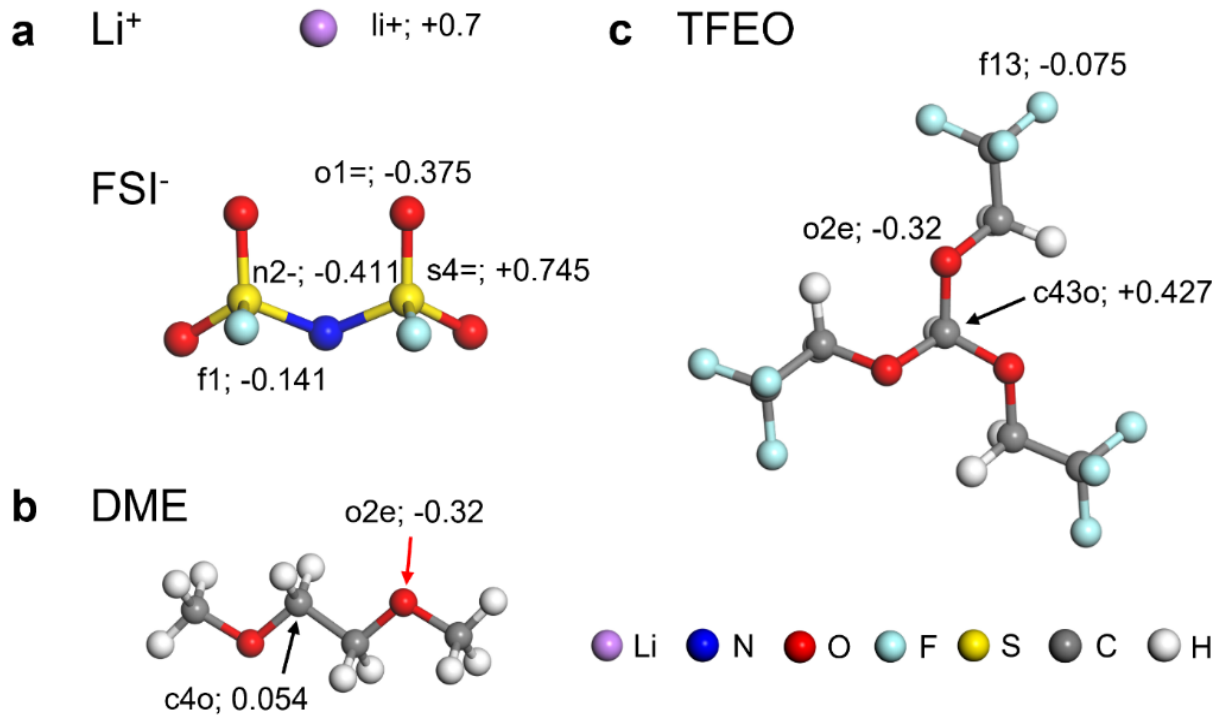

Supplementary Fig. 18 | Atom types and atomic charges used in MD simulations. Representative atom types and atomic charges in **a**, LiFSI, **b**, DME, and **c**, TFEO used in MD simulations. Note that all atomic charges in LiFSI are scaled by 0.7 to account for the ion-ion and ion-dipole interactions.

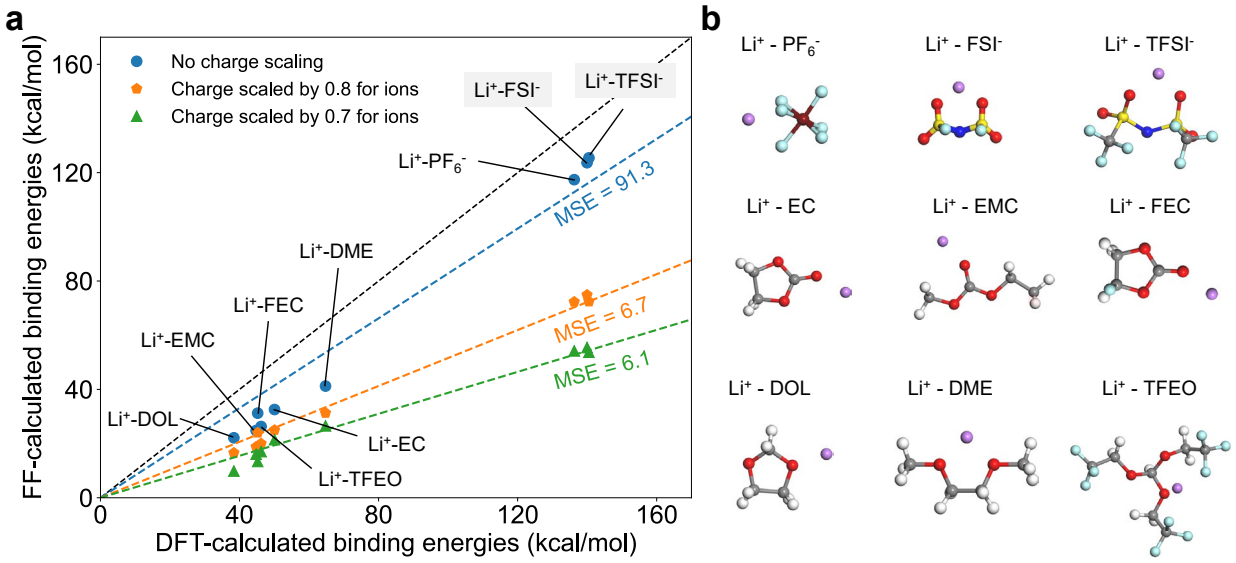

Supplementary Fig. 19 | DFT- vs force field (FF)-calculated binding energies. a, Binding energies calculated based on COMPASS III force field (FF) as functions of binding energies calculated based on DFT method. Binding energy (BE) is defined as $E_{BE} = E_{Li^+} + E_{mol} - E_{bound}$, where E_{Li^+} denotes the energy of Li^+, E_{mol} denotes the energy of the molecular species (salt anion, solvent or diluent), and E_{bound} denotes the energy of the bound system. Blue dots refer to the FF-calculated binding energies without charge scales, while orange and green dots refer to the binding energies calculated based on charge scales of 0.8 and 0.7, respectively. The blue, orange, and green dash lines correspond to linear fittings with intercept of zero. It is seen that the mean squared errors (MSE, in kcal/mol) of the linear fittings are largely reduced with charge scales of 0.8 and 0.7, which indicate the cation-anion and cation-solvent interactions become more balanced. **b**, atomic structures of Li^+-coordinated species. Gray, white, red, light blue, purple, brown, yellow, and dark blue atoms represent C, H, O, F, Li, P, S, and N atoms, respectively.

Supplementary Tables 3, 4 and 5 list the molar ratio, number of salt and solvent species in the simulation cell, scaled charge, temperature, simulation cell size, salt concentration, density, Li^+ diffusivity, Li^+ conductivity, and Li^+ coordination numbers with O/F atoms in salt anions and solvents. For calculations of coordination numbers, we used a cutoff of 2.8 Å. Note that the blue texts in brackets are experimentally measured data and the red texts in brackets are MD-simulated data with APPLE&P force field by Oleg Borodin and Grant D. Smith.[16] In Supplementary Table 3 and Table 4, both the experimental and simulation data are taken from Qian et al.[17] The experimental data was obtained at 25 °C and the MD simulations with APPLE&P force field were conducted at 60 °C. In Supplementary Table 5, the experimentally measured data (for the 1 M $LiPF_6$ in EC-EMC-DEC (2-2-1 by mole) electrolyte) and the APPLE&P force field simulated data is from Hayashi et al.[18] and Borodin and Smith,[16] both of which were obtained at 25 °C.

Supplementary Table 3 | MD data of LCE (1 M LiFSI in DME).

Simulated electrolyte		1M LiFSI-DME					
Molar ratio (DME:LiFSI)		9:1 (9:1) (8.9:1)					
# of DME and LiFSI in simulation cell		360 DME and 40 LiFSI (576 DME and 64 LiFSI)					
Charge scale of LiFSI		**0.8**			**0.7**		
Temperature (ºC)		-20	20	60	-20	20	60
Simulation cell size (Å)		39.4	39.9	40.5	39.4	39.9	40.5
Concentration (M)		1.09	1.05	1.00 (0.96)	1.09	1.04	1.00 (0.96)
Density (g/cm^3)		1.09	1.04	1.00 (0.96)	1.08	1.04	1.00 (0.96)
Li^+ diffusivity (×10^{-10} m^2/s)		0.66	2.29	5.04	1.21	3.99	7.60
Li^+ conductivity (mS/cm)		3.20	9.14 (16.9)	17.0 (23.2)	5.81	**15.9** (16.9)	**25.6** (23.2)
coordination number (cutoff: 2.8 Å)	total (Li-O/F)	5.75	5.52	5.23	5.63	5.31	5.03
	Li-O(DME)	4.77	4.29	3.70 (4.42)	5.52	4.93	**4.50** (4.42)
	Li-O(FSI)	0.98	1.22	1.52 (0.42)	0.11	0.37	**0.52** (0.42)
	Li-F	0.00	0.01	0.01	0.00	0.01	0.01

Supplementary Table 4 | MD data of HCE (4 M LiFSI in DME).

Simulated electrolyte		4M LiFSI-DME					
Molar ratio (DME:LiFSI)		1.4:1 (1.4:1) (1.4:1)					
# of DME and LiFSI in simulation cell		288 DME and 200 LiFSI (488 DME and 320 LiFSI)					
charge scale of LiFSI		**0.8**			**0.7**		
Temperature (ºC)		-20	20	60	-20	20	60
Simulation cell size (Å)		40.8	41.1	41.4	41.0	41.3	41.7
Concentration (M)		4.88	4.78	**4.68** (4.24)	4.82	4.72	**4.59** (4.24)
density (g/cm^3)		1.53	1.50	1.47 (1.33)	1.53	1.48	1.47 (1.33)
Li^+ diffusivity ($\times10^{-10}$ m^2/s)		0.003	0.018	0.053	0.01	0.047	0.38
Li^+ conductivity (mS/cm)		0.072	0.33 (5.7)	**0.84** (4.2)	0.21	0.84 (5.7)	**5.82** (4.2)
coordination number (cutoff: 2.8 Å)	total (Li-O/F)	5.35	5.20	5.11	5.18	5.07	4.99
	Li-O(DME)	2.17	2.15	2.07 (2.60)	2.14	2.49	2.02 (2.60)
	Li-O(FSI)	3.12	3.00	2.98 (1.92)	2.98	2.51	2.91 (1.92)
	Li-F	0.06	0.05	0.06	0.06	0.07	0.06

Supplementary Tables 5 | MD data of 1M $LiPF_6$ in EC-EMC (3-7 by vol).

Simulated electrolyte		1M $LiPF_6$-EC:EMC(3:7, v:v)					
Molar ratio (EC:EMC:$LiPF_6$)		13:20:3					
# of EC, EMC and $LiPF_6$		156 EC, 240 EMC and 36 $LiPF_6$					
charge scale of $LiPF_6$		**0.8**			**0.7**		
Temperature (ºC)		-20	20	60	-20	20	60
Simulation cell size (Å)		39.0	39.5	40.0	39.1	39.6	40.1
Concentration (M)		1.01	0.97	0.93	1.00	0.96	0.93
Density (g/cm^3)		1.23	1.19	1.14	1.22	1.18	1.14
Li^+ diffusivity (×10^{-10} m^2/s)		0.70	2.52 (~3.5)	4.98	1.06	3.48 (~3.5)	9.04
Li^+ conductivity (mS/cm)		3.10	**9.32** (~10) (~ 11)	15.6	4.68	**12.8** (~10) (~ 11)	28.2
coordination number (cutoff: 2.8 Å)	total (Li-O/F)	5.01	4.91	4.85	4.61	4.54	4.48
	Li-O(EC)	2.58	2.35	2.27	2.48	2.29	2.18
	Li-O(EMC)	1.82	1.74	1.52	1.86	1.78	1.67
	Li-F	0.61	0.82	1.06	0.27	0.47	0.63

Supplementary Table 6 | MD-calculated ratios of SSIP, CIP, AGG and AGG+ that are obtained using scaled charges of 0.7 and 0.8, as well as through Raman deconvolution analysis. It is seen that scaled charge of 0.7 gives reasonable description of ion pairing and aggregation for both LCE and HCE when compared to Raman data. The SSIP ratio is significantly underestimated with a scaled charge of 0.8 in LCE when compared to Raman data.

Electrolyte	Method	SSIP	CIP	AGG	AGG+
LCE (LiFSI-9DME)	MD (Scale: 0.7)	0.733	0.242	0.025	0.000
	MD (Scale: 0.8)	0.185	0.376	0.424	0.015
	Raman	0.646	0.279	0.075	0.000
HCE (LiFSI-1.4DME)	MD (Scale: 0.7)	0.024	0.131	0.629	0.216
	MD (Scale: 0.8)	0.010	0.065	0.621	0.304
	Raman	0.032	0.137	0.543	0.288

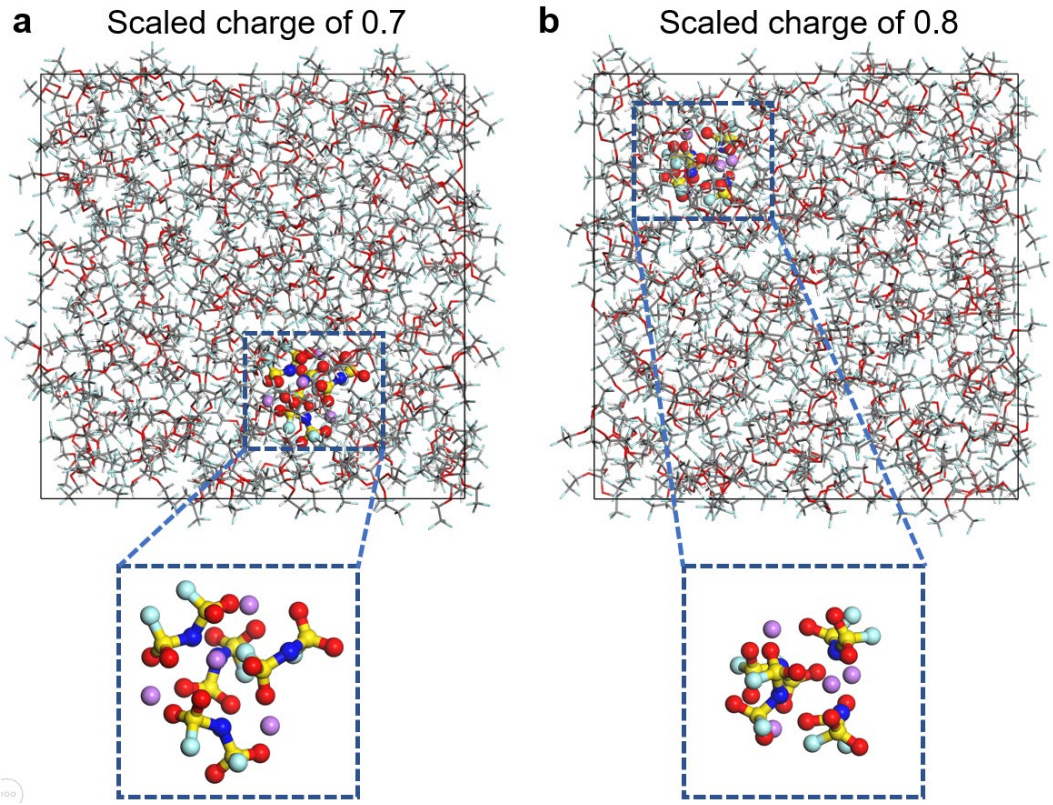

Supplementary Fig. 20 | MD-simulated structure of 4 LiFSI molecules in TFEO matrix (with 200 TFEO molecules) for different scaled charges. Scaled charge of **a,** 0.7 and **b**, 0.8, where in both simulations the cations and anions were initially uniformly separated in the TFEO diluent. By the end of the simulation (22.0 ns under NPT ensemble at room temperature, 25 °C), the anions and cations formed salt clusters (with 4 Li^+ and 4 FSI^-). Both simulations reveal no solvation of LiFSI salt in TFEO, suggesting that the scaled charge of 0.7 or 0.8 makes no difference in balancing the ion charges and partial charges with TFEO diluent.

2. Simulation Systems

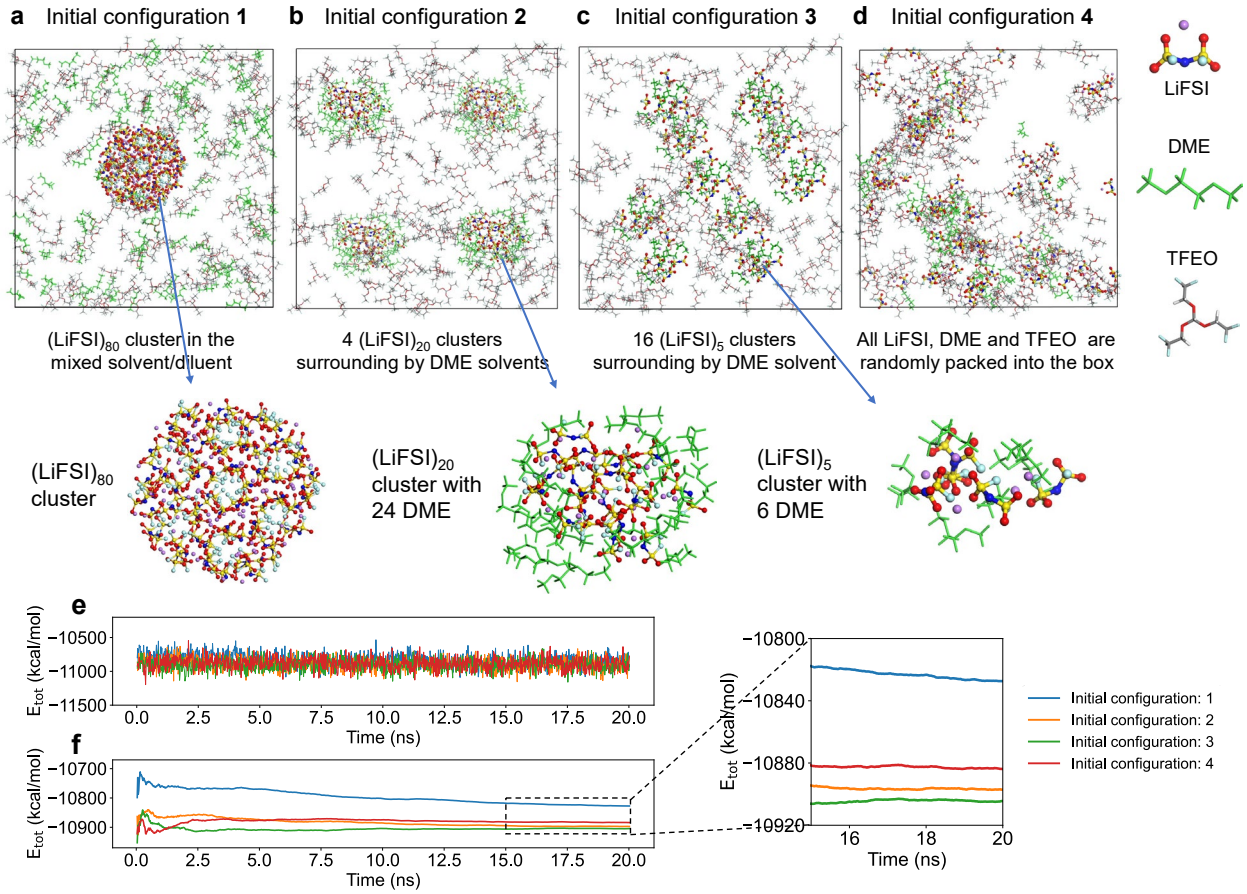

Supplementary Fig. 21 | MD simulations of LHCE starting from several different initial configurations. **a**, Initial configuration 1 for MD simulations starting from immersing LiFSI cluster (80 LiFSI molecules, i.e., $(LiFSI)_{80}$) into the mixed DME solvent and TFEO diluent. **b**, Initial configuration 2 for MD simulations starting with 4 $(LiFSI)_{20}$ clusters surrounding by DME solvents and then TFEO diluent. **c**, Initial configuration 3 for MD simulations starting with 16 $(LiFSI)_5$ clusters surrounding by DME solvents and then TFEO diluent. **d**, Initial configuration 4 for MD simulations starting with all LiFSI, DME and TFEO being randomly packed into the simulation box. All MD simulations were conducted with same number of species (80 LiFSI, 96 DME and 160 TFEO) and same initial simulation box size ($80\times80\times80$ Å^3) at the same temperature (25 ℃). **e**, Evolutions of total energies and **f**, time-averaged total energies of MD simulations with different initial configurations (1-4). It is seen that the MD simulation starting with initial configuration 3 gives the lowest total energy, and thus adopted for MD simulations at other temperatures as well.

Supplementary Table 7 | Table list of number of LiFSI, DME, and/or TFEO in the simulation cells of different systems for MD simulations.

System	LiFSI	DME	TFEO
LHCE (LiFSI-1.2DME-2TFEO)	80	96	160
HCE (LiFSI-1.2DME)	200	240	-
HCE (LiFSI-1.4DME)	200	280	-
LCE (LIFSI-9DME)	40	360	-
DME-TFEO (DME-2TFEO)	-	96	160
LiFSI-TFEO (LiFSI:TFEO → 0)	4	-	200
LiFSI crystal	432	-	-

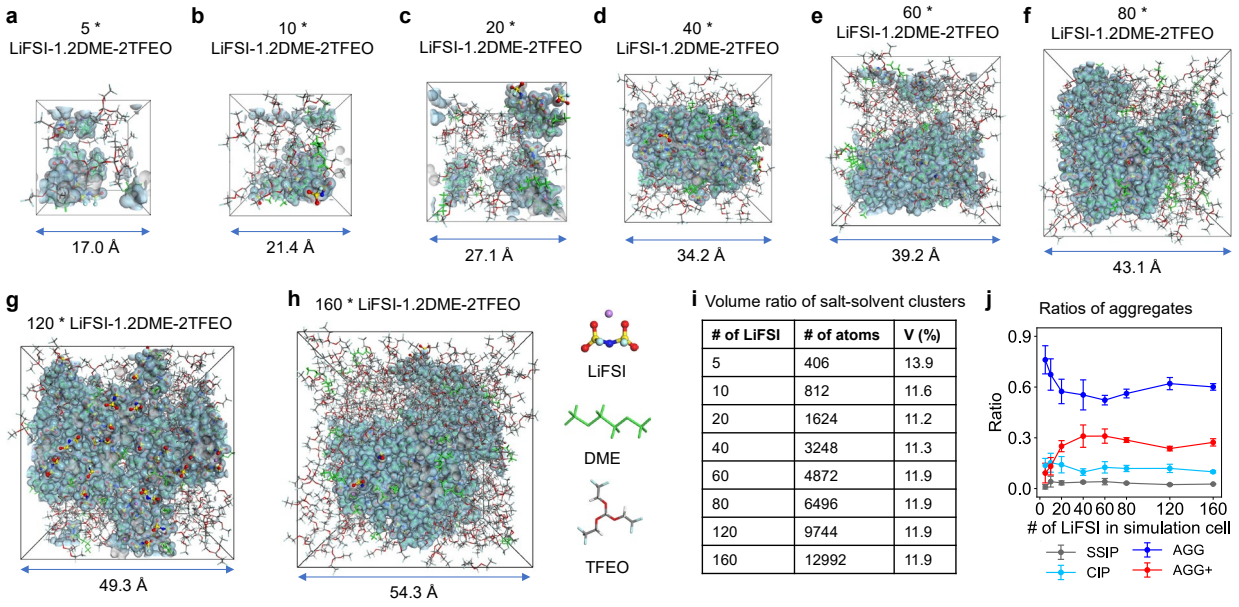

# of LiFSI	# of atoms	V (%)
5	406	13.9
10	812	11.6
20	1624	11.2
40	3248	11.3
60	4872	11.9
80	6496	11.9
120	9744	11.9
160	12992	11.9

Supplementary Fig. 22 | Perspective views of MD simulations using different simulation cells at room temperature for LHCE (LiFSI-1.2DME-2TFEO). **a**, 5 * LiFSI-1.2DME-2TFEO with a box size of 17.0 Å on each side; **b**, 10 * LiFSI-1.2DME-2TFEO with a box size of 21.4 Å; **c**, 20 * LiFSI-1.2DME-2TFEO with a box size of 27.1 Å; **d**, 40 * LiFSI-1.2DME-2TFEO with a box size of 34.2 Å; **e**, 60 * LiFSI-1.2DME-2TFEO with a box size of 39.2 Å; **f**, 80 * LiFSI-1.2DME-2TFEO with a box size of 43.1 Å; **g**, 120 * LiFSI-1.2DME-2TFEO with a box size of 49.3 Å; **h**, 160 * LiFSI-1.2DME-2TFEO with a box size of 54.3 Å. The vdW surfaces are shown accordingly. The salt-solvent clusters are highlighted through drawing their vdW surfaces. **i**, Number of LiFSI and atoms, as well as volume ratios of the salt-solvent clusters for LHCE with different simulation cells. **j**, Ratios of aggregates (SSIP, CIP, AGG and AGG+) for LHCE with different simulation cells. All the reported values in **d** are averaged for 4 ns production run, $\langle probability(4\,ns)\rangle$, with n>10,000 (number of MD frames multiplying number of LiFSI molecules in the systems). We define the error bar as the difference between the maximum and minimum in the time-averaged values, $error = \pm(\,max\{\langle probability(t)\rangle\} - min\{\langle probability(t)\rangle\})$, from 2 ns to 4 ns during production runs.

3. Statistics of MD results

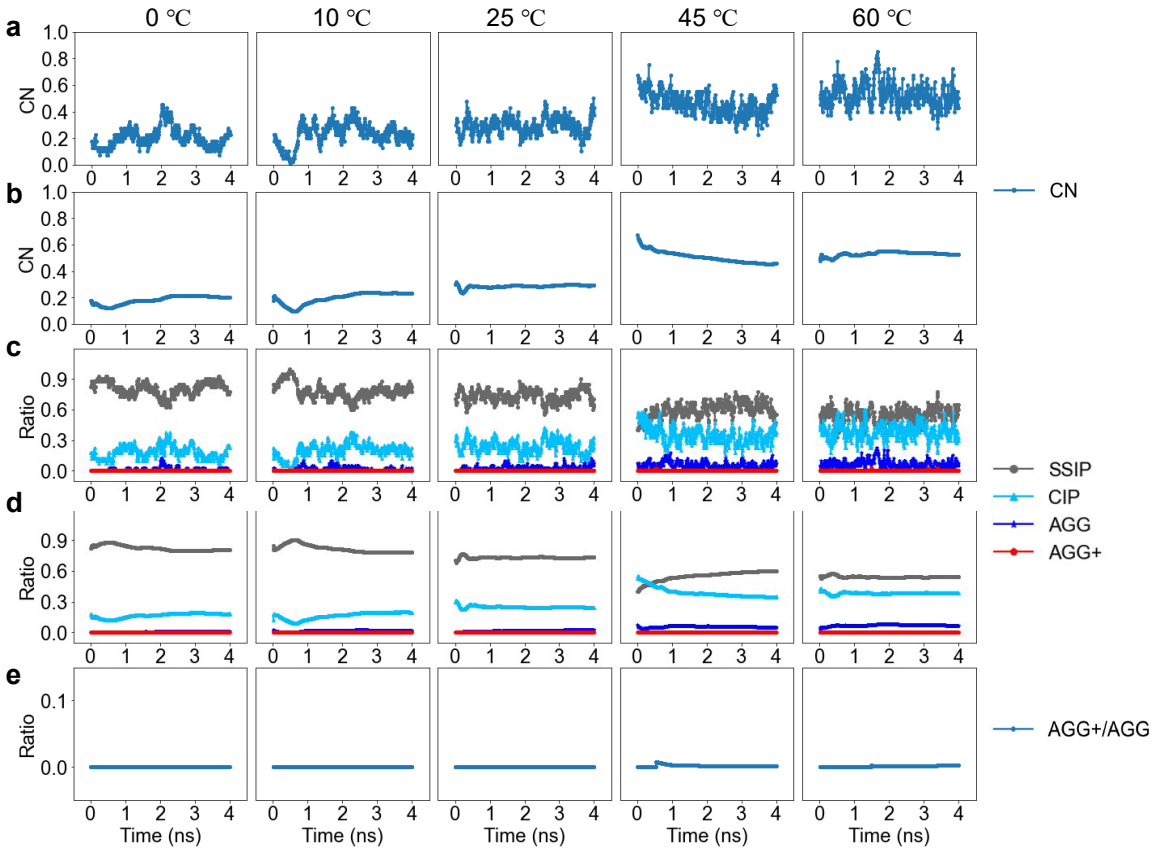

Supplementary Fig. 23 | Statistics of coordination numbers (CN) and aggregation ratios for LCE (LiFSI-9DME). **a**, MD-calculated FSI^- *vs* Li^+ CN as function of time during production runs (the last 4 ns simulations). **b**, Time-averaged FSI^- *vs* Li^+ CN as function of time. **c**, MD-calculated aggregation ratios (SSIP, CIP, AGG and AGG+) as function of time. **d**, Time-averaged aggregation ratios (SSIP, CIP, AGG and AGG+) as function of time. **e**, AGG+/AGG ratio as function of time.

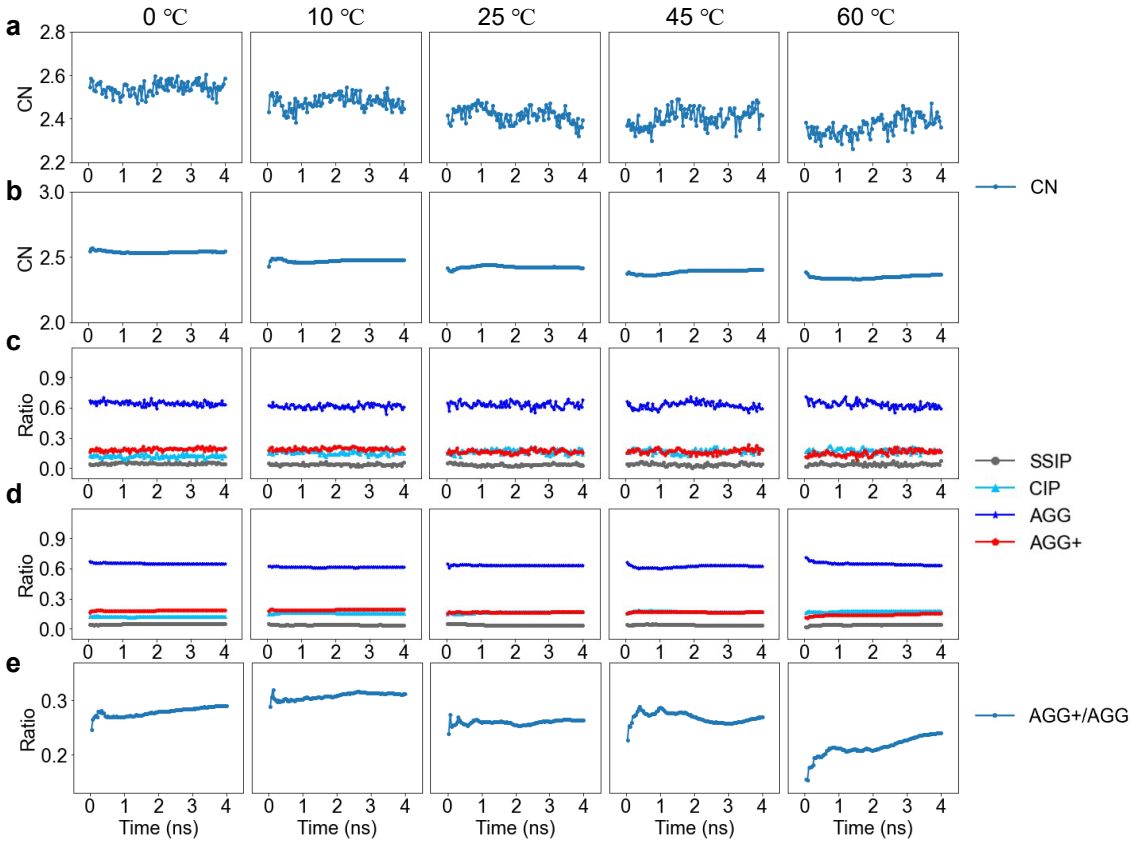

Supplementary Fig. 24 | Statistics of coordination numbers (CN) and aggregation ratios for HCE (LiFSI-1.4DME). **a**, MD-calculated FSI^- *vs* Li^+ CN as function of time during production runs (the last 4 ns simulations). **b**, Time-averaged FSI^- *vs* Li^+ CN as function of time. **c**, MD-calculated aggregation ratios (SSIP, CIP, AGG and AGG+) as function of time. **d**, Time-averaged aggregation ratios (SSIP, CIP, AGG and AGG+) as functions of time. **e**, AGG+/AGG ratio as functions of time.

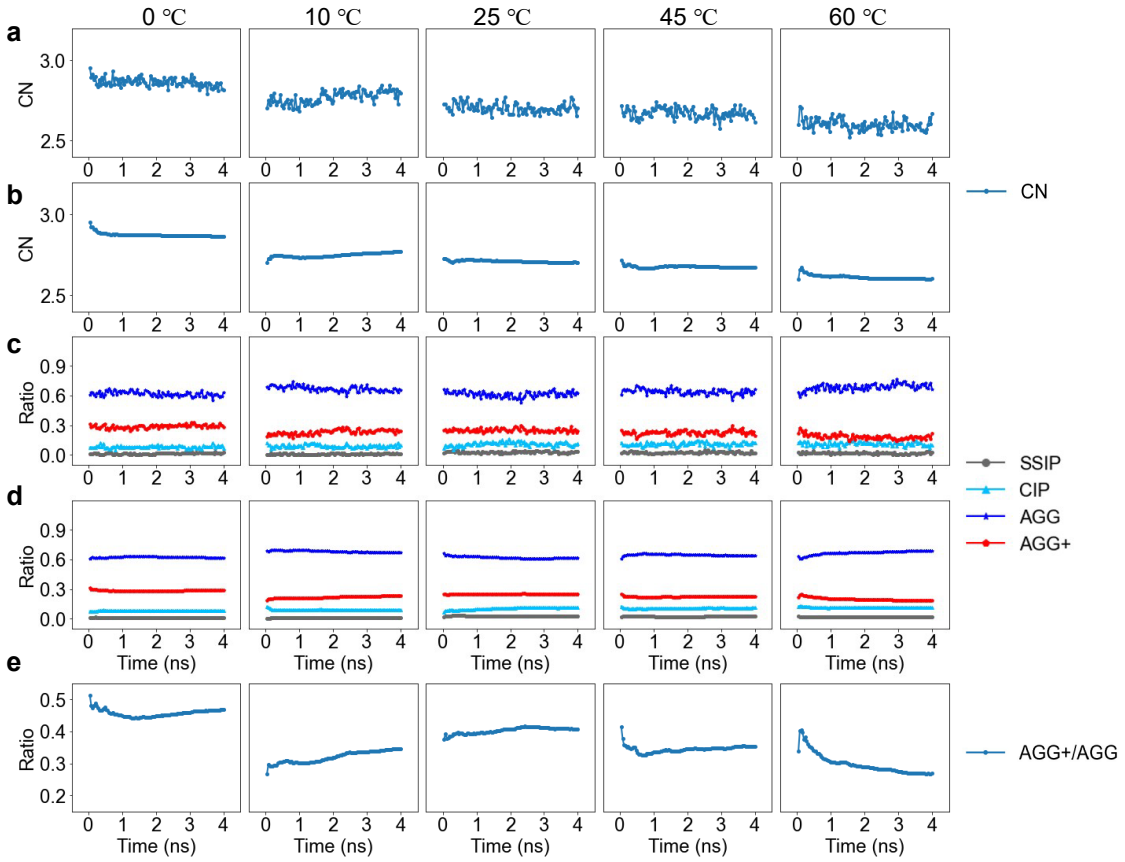

Supplementary Fig. 25 | Statistics of coordination numbers (CN) and aggregation ratios for HCE (LiFSI-1.2DME). **a**, MD-calculated FSI^- *vs* Li^+ CN as function of time during production runs (the last 4 ns simulations). **b**, Time-averaged FSI^- *vs* Li^+ CN as function of time. **c**, MD-calculated aggregation ratios (SSIP, CIP, AGG and AGG+) as function of time. **d**, Time-averaged aggregation ratios (SSIP, CIP, AGG and AGG+) as function of time. **e**, AGG+/AGG ratio as function of time.

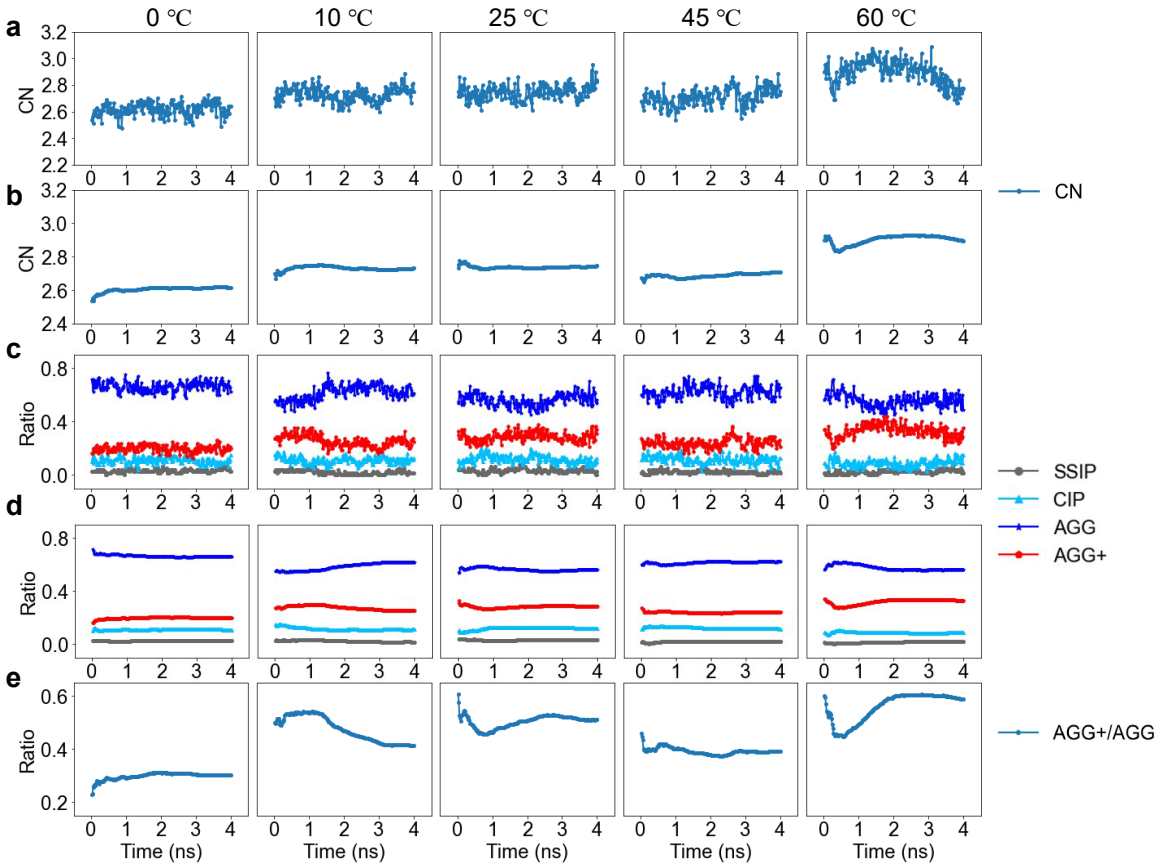

Supplementary Fig. 26 | Statistics of coordination numbers (CN) and aggregation ratios for LHCE (LiFSI-1.2DME-2TFEO). **a**, MD-calculated FSI^- *vs* Li^+ CN as function of time during production runs (the last 4 ns simulations). **b**, Time-averaged FSI^- *vs* Li^+ CN as function of time. **c**, MD-calculated aggregation ratios (SSIP, CIP, AGG and AGG+) as function of time. **d**, Time-averaged aggregation ratios (SSIP, CIP, AGG and AGG+) as function of time. **e**, AGG+/AGG ratio as function of time.

4. Additional Convergence test for LHCE

The error bars are generally small in homogenous LCE and HCE and become larger in heterogenous LHCE. Thus, additional 10 ns NPT dynamics are run (Supplementary Fig. 25). The conclusion holds considering the error bars, including the occurrence of a peak value of AGG+/AGG at room temperature, which show larger scattering. This is likely due to the smaller cluster sizes in MD simulations compared to experiments.

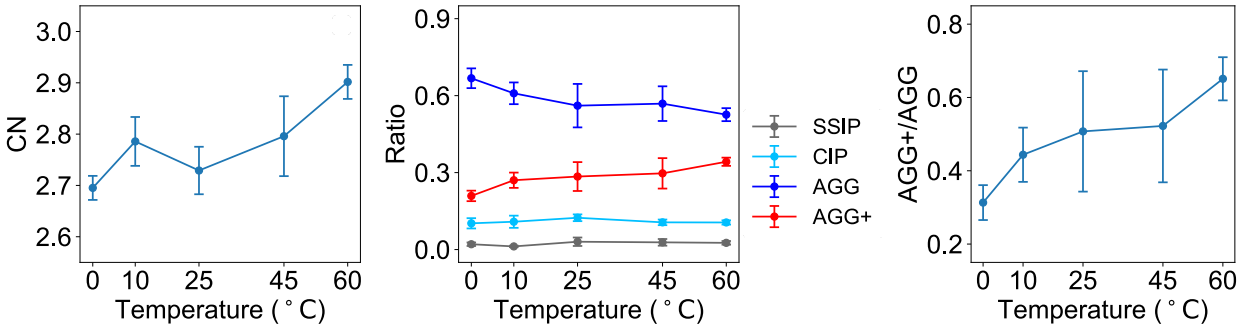

Supplementary Fig. 27 | Time-averaged coordination number (CN) and aggregate types as a function of temperature for an extended 10.0 ns NPT simulation of LHCE (LiFSI-1.2DME-2TFEO). a, Time-averaged FSI^- *vs* Li^+ CN, **b**, ratios of aggregates (SSIP, CIP, AGG and AGG+), and **c**, AGG+/AGG ratios. All the reported values are averaged for 10 ns production run, $\langle probability(10\ ns)\rangle$, with n=16,000 (200 frames multiplying 80 LiFSI molecules). We define the error bar as the difference between the maximum and minimum in the time-averaged values, $error = \pm(\ max\{\langle probability(t)\rangle\} - min\{\langle probability(t)\rangle\})$, from 5 ns to 10 ns during production runs.

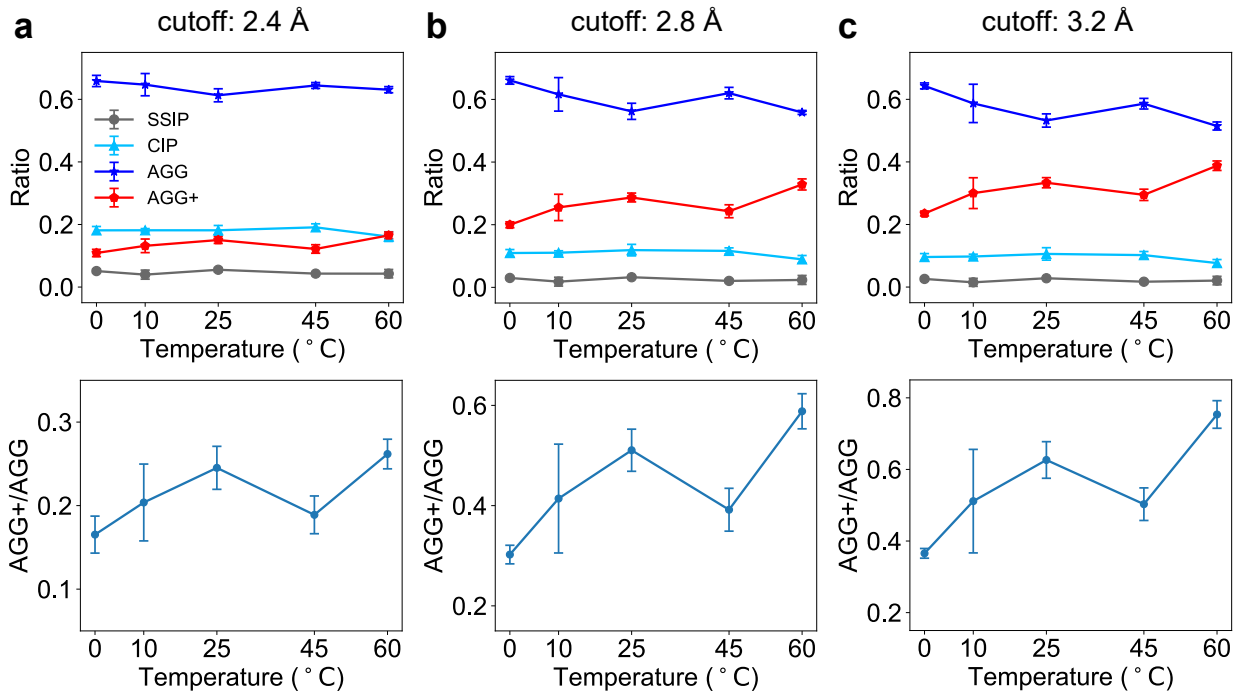

Supplementary Fig. 28 | MD tests on different cutoffs used for calculating salt-solvent cluster ratios. Calculated ratios (upper panels) of SSIP, CIP, AGG, and AGG+ as a function of temperature, as well as AGG+/AGG ratio (lower panels) as a function of temperature using the cutoff of **a**, 2.4 Å, **b**, 2.8 Å and **c**, 3.2 Å. It is seen that the trend does not change using different cutoffs (2.4 Å, 2.8 Å and 3.2 Å) when calculating the ratios of aggregates. The cutoff of 2.8 Å is used in this work. LHCE (LiFSI-1.2DME-2TFEO) was used to exemplify the chosen cutoff. All the reported values are averaged for 4 ns production run, $\langle probability(4\ ns)\rangle$, with n=16,000 (200 frames multiplying 80 LiFSI molecules). We define the error bar as the difference between the maximum and minimum in the time-averaged values, $error = \pm(\ max\{\langle probability(t)\rangle\} - min\{\langle probability(t)\rangle\})$, from 2 ns to 4 ns during production runs.

References

1 Cao, X. *et al.* Optimization of fluorinated orthoformate based electrolytes for practical high-voltage lithium metal batteries. *Energy Storage Mater* **34**, 76-84, doi:10.1016/j.ensm.2020.08.035 (2021).

2 Su, L. S. *et al.* Uncovering the Solvation Structure of LiPF6-Based Localized Saturated Electrolytes and Their Effect on LiNiO2-Based Lithium-Metal Batteries. *Adv Energy Mater* **12**, doi:10.1002/aenm.202201911 (2022).

3 Adams, B. D., Zheng, J. M., Ren, X. D., Xu, W. & Zhang, J. G. Accurate Determination of Coulombic Efficiency for Lithium Metal Anodes and Lithium Metal Batteries. *Adv Energy Mater* **8**, doi:10.1002/aenm.201702097 (2018).

4 Piao, N. *et al.* Countersolvent Electrolytes for Lithium-Metal Batteries. *Adv Energy Mater* **10**, doi:10.1002/aenm.201903568 (2020).

5 Cao, X. *et al.* Effects of fluorinated solvents on electrolyte solvation structures and electrode/electrolyte interphases for lithium metal batteries. *P Natl Acad Sci USA* **118**, doi:10.1073/pnas.2020357118 (2021).

6 Cao, X. *et al.* Monolithic solid-electrolyte interphases formed in fluorinated orthoformate-based electrolytes minimize Li depletion and pulverization. *Nat Energy* **4**, 796-805, doi:10.1038/s41560-019-0464-5 (2019).

7 Ren, X. D. *et al.* Enabling High-Voltage Lithium-Metal Batteries under Practical Conditions. *Joule* **3**, 1662-1676, doi:10.1016/j.joule.2019.05.006 (2019).

8 Hou, Z. P. *et al.* Protecting Li Metal Anode While Suppressing "Shuttle Effect" of Li-S Battery Through Localized High-Concentration Electrolyte. *J Electron Mater* **51**, 4772-4779, doi:10.1007/s11664-022-09751-z (2022).

9 Chen, S. R. *et al.* High-Voltage Lithium-Metal Batteries Enabled by Localized High-Concentration Electrolytes. *Adv Mater* **30**, doi:10.1002/adma.201706102 (2018).

10 Liu, T. *et al.* Low-Density Fluorinated Silane Solvent Enhancing Deep Cycle Lithium-Sulfur Batteries' Lifetime. *Adv Mater* **33**, doi:10.1002/adma.202102034 (2021).

11 Zheng, J. *et al.* High-Fluorinated Electrolytes for Li-S Batteries. *Adv Energy Mater* **9**, doi:10.1002/aenm.201803774 (2019).

12 Tan, S. *et al.* Isoxazole-Based Electrolytes for Lithium Metal Protection and Lithium-Sulfurized Polyacrylonitrile (SPAN) Battery Operating at Low Temperature. *J Electrochem Soc* **169**, doi:10.1149/1945-7111/ac58c5 (2022).

13 Huangzhang, E. *et al.* A localized high-concentration electrolyte with lithium bis(fluorosulfonyl) imide (LiFSI) salt and F-containing cosolvents to enhance the performance of Li||LiNi0.8Co0.1Mn0.1O2 lithium metal batteries. *Chem Eng J* **439**, doi:10.1016/j.cej.2022.135534 (2022).

14 Chen, S. R. *et al.* High-Efficiency Lithium Metal Batteries with Fire-Retardant Electrolytes. *Joule* **2**, 1548-1558, doi:10.1016/j.joule.2018.05.002 (2018).

15 Ren, X. D. *et al.* Localized High-Concentration Sulfone Electrolytes for High-Efficiency Lithium-Metal Batteries. *Chem-Us* **4**, 1877-1892, doi:10.1016/j.chempr.2018.05.002 (2018).

16 Borodin, O. & Smith, G. D. Quantum Chemistry and Molecular Dynamics Simulation Study of Dimethyl Carbonate: Ethylene Carbonate Electrolytes Doped with LiPF6. *J Phys Chem B* **113**, 1763-1776, doi:10.1021/jp809614h (2009).

17 Qian, J. F. *et al.* High rate and stable cycling of lithium metal anode. *Nat Commun* **6**, doi:10.1038/ncomms7362 (2015).

18 Hayashi, K., Nemoto, Y., Tobishima, S. & Yamaki, J. Electrolyte for high voltage Li/LiMn1.9Co0.1O4 cells. *J Power Sources* **68**, 316-319, doi:10.1016/S0378-7753(97)02636-0 (1997).